Geological Magazine

www.cambridge.org/geo

Omission and pacing of events at the Norian–Rhaetian and Triassic–Jurassic transitions in Britain

Mark W. Hounslow[1,2], Paulette E. Posen[3], Geoffrey Warrington[4] and Kevin N. Page[5,6]

[1]Lancaster Environment Centre, Lancaster University, Lancaster, UK; [2]Earth, Ocean and Ecological Sciences, Univ. of Liverpool, Jane Herdman Building, Liverpool, UK; [3]School of Environmental Sciences, University of East Anglia, Norwich, UK; [4]School of Geography, Geology and the Environment, University of Leicester, University Road, Leicester, UK; [5]Geodiversity & Heritage, Sandford, Devon, UK and [6]Camborne School of Mines, University of Exeter, Penryn, Cornwall, UK

Original Article

Cite this article: Hounslow MW, Posen PE, Warrington G, and Page KN. Omission and pacing of events at the Norian–Rhaetian and Triassic–Jurassic transitions in Britain. *Geological Magazine* **162**(e27): 1–27. https://doi.org/10.1017/S0016756825100162

Received: 5 November 2024
Revised: 17 March 2025
Accepted: 15 July 2025

Keywords:
ammonite biochronology; palynology; magnetostratigraphy; astrochronology; cyclostratigraphy; Triassic–Jurassic boundary

Corresponding author:
Mark W Hounslow;
Email: m.hounslow@lancaster.ac.uk

Abstract

Magnetostratigraphy, palynology and ammonite biochronology of the Staithes S-20 core are used in an integrated evaluation of the late Norian to early Hettangian successions in Britain. The polarity patterns of the Blue Anchor and Westbury formations differ from their counterparts in SW England, indicating younger and older ages, respectively, for those units in NE England. Magnetostratigraphy indicates an underlying Sevatian age hiatus coeval with the D5 disconformity of the German Keuper. The miospore succession from S-20 is divisible into zones like those from the St Audrie's Bay section in SW England. Using magnetic susceptibility datasets for the earliest Hettangian chronozones from S-20, Lavernock, St Audrie's Bay and Lyme Regis, a new method is used to derive a TimeOpt-based astrochronology for the earliest Hettangian. This is anchored to radioisotopic dates from Peru correlated into British sections using carbon isotope excursions. A brief reverse magnetozone in the basal Cotham Member in the Staithes S-20 core and the astrochronological evaluation demonstrate that CAMP volcanics are coeval with the end-Triassic extinction in UK sections. An eco-plant model assessment of the miospores indicates greater proportions of eurythermic and europhyte floras, suggesting stronger seasonality in palaeoclimate was probably a key factor in the end-Triassic extinction.

1. Introduction

Unravelling the causes and consequences of major rapid environmental changes requires a detailed understanding of the timing of key events, often observed in sedimentary basins on different continents. The timing of events at the Triassic–Jurassic boundary (the Rhaetian–Hettangian boundary) has been increasingly refined using a combination of carbon isotope stratigraphy, geochronology, magnetostratigraphy and biostratigraphy. This has allowed the timing of the eruption of the Central Atlantic Magmatic Province (CAMP) flood basalts and events in marine sediments to be better understood (Clémence *et al.*, 2010; Boomer *et al.*, 2021; Lindström *et al.*, 2017, 2023; Yager *et al.*, 2021; Zaffani *et al.*, 2018), suggesting a two-phased extinction (Lindström, 2021). However, some datasets suggest alternative scenarios (Fox *et al.*, 2020; Beith *et al.*, 2023).

In the UK, the Norian–Rhaetian to early Hettangian interval is a transition from red-green playa mudstones in the upper part of the Mercia Mudstone Group (MMG), though the Penarth Group (Benton *et al.*, 2002; Gallois, 2007; 2009) and into the marine units of the lowest Lias Group (Gp; Fig. 1b). This lithostratigraphical framework is generally consistent throughout England (Benton *et al.*, 2002), Northern Ireland (Warrington, 1997) and into the southern North Sea (Lott and Warrington, 1988; Johnson *et al.*, 1994; Barnasch *et al.*, 2021). Comparable units occur in the central and eastern parts of the southern Permian Basin (Bachmann *et al.*, 2010; Fig. 1b). Some of these Rhaetian-age units contain macrofossils, but these do not generally provide sufficiently precise biostratigraphic dating. However, Rhaetian palynostratigraphy allows fairly detailed correlations within NW Europe (Bonis *et al.*, 2010; Lindström & Erlström, 2006; Kürschner & Herngreen, 2010; Lindström *et al.*, 2017), although magnetostratigraphy and carbon isotope stratigraphy have the potential to provide a finer-scale chronostratigraphy and correlation in the Rhaetian (Gallet *et al.*, 2007; Kent *et al.*, 2017; Hounslow & Andrews, 2024). In the UK, Hettangian units are well-dated by ammonoids, except for the lower parts of the Tilmanni Chronozone (Cz) of the basal Hettangian (Page, 2003, 2010; Weedon *et al.*, 2018, 2019), the base of which outside the GSSP at Kuhjoch can only be inferred by correlations using carbon isotopes, miospores and geochemical datasets.

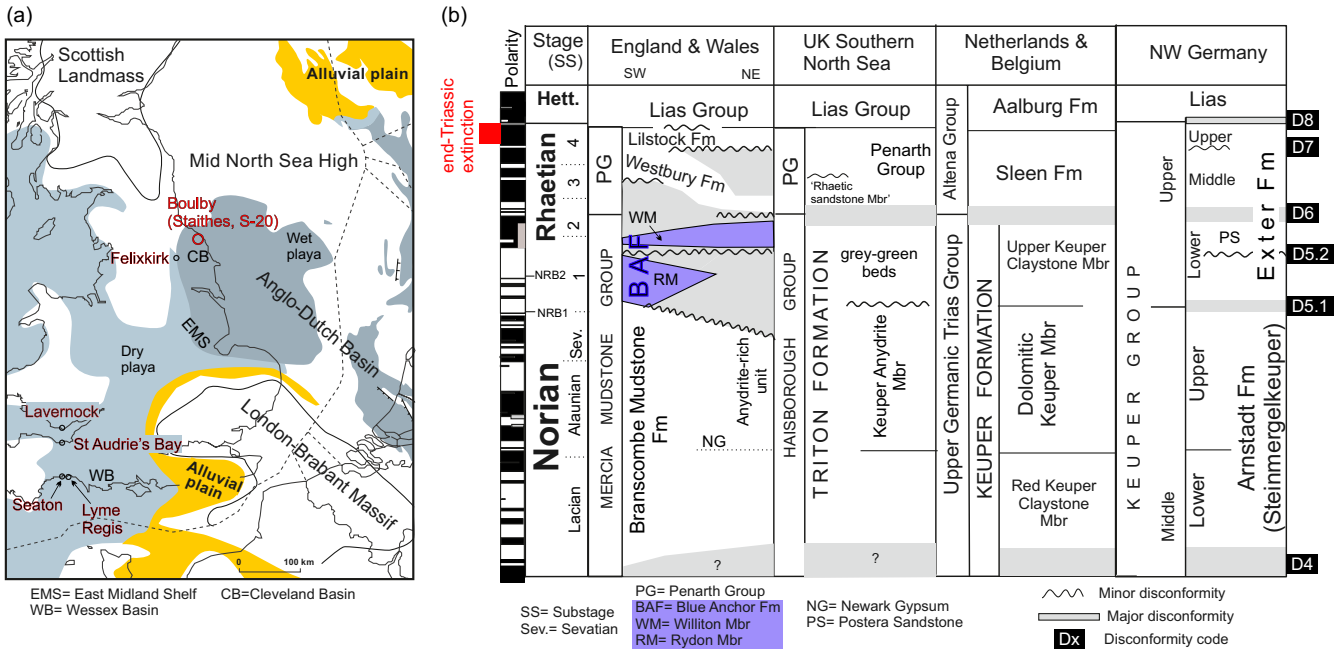

Figure 1. a) Summary map of locations and environmental facies for the interval occupied by the Branscombe Mudstone Fm and its equivalents. The Staithes S-20 borehole is located at Boulby. Base map modified from Geluk (2005), with facies concepts from McKie (2014); b) Summary lithostratigraphy for England from this work, with that for the southern North Sea region from Cameron *et al.* (1992); other correlations and disconformities based on Barnasch (2010), Hounslow & Andrews (2024) and this work. Summary polarity and substage scale from Hounslow & Gallois (2023). Numbered subdivisions of the Rhaetian based on Krystyn (2008). NRB1 and NRB2 are the two proposed options for the position of the Norian–Rhaetian boundary.

The late Rhaetian–early Hettangian succession in southern England and Northern Ireland has been well studied using a variety of methods (Boomer *et al.*, 2021), but comparatively little detailed work has been carried out on successions in northern England, Scotland or the UK North Sea. This omission is addressed here using magnetostratigraphy, biostratigraphy and astrochronology of the succession from the Staithes No. 20 core from the Boulby Mine in NE England (hereafter called S-20; Fig. 1a). The Norian-age eastern England successions were key for detailed initial studies of this interval in the UK (Elliott, 1961; Taylor, 1982), but the paucity of later studies was superseded by work on better outcrop exposures in SW England. The Rhaetian age units in eastern and NE England have remained less studied, since these are largely known from boreholes and temporary exposures (Kent 1953; 1968). An aim of this study is to clarify the regional relationships of Norian and Rhaetian units in NE and eastern England, which have been correlated using borehole logs across the southern North Sea to Germany (Barnasch, 2010). In addition, magnetic susceptibility data from the earliest Hettangian part of the S-20 core allows a re-evaluation of conflicting views (Ruhl *et al.*, 2010; Weedon *et al.*, 2019) on the cyclostratigraphy and duration of the early Hettangian, specifically for the Tilmanni Cz and the Planorbis Subchronozone (Scz).

1.a. Uncertainty in the definition of the Norian–Rhaetian boundary

Where to place the Norian–Rhaetian boundary is undecided, and two proposals have been suggested (positions here called NRB1 and NRB2; Fig. 1b). These differ significantly in chronostratigraphic position and use different points in the morphological change of the conodont *Misikella posthernsteini* from its ancestor *Misikella hernsteini* (Galbrun *et al.*, 2020). Subdivisions of the Rhaetian into informal units 1 to 4 are used here, based on the conodont ranges and zones of Krystyn (2008) and Galbrun *et al.* (2020). Rhaetian-1 starts from the base of the Rhaetian as defined by Krystyn et al. (2007) and referred to as NRB1 and ranges through the base of the Rhaetian as proposed by Rigo *et al.* (2016), referred to as NRB2; this is the *Epigondolella bidentata–M. posthernsteini* Zone. Rhaetian-2 is the *M. posthernsteini–M. hernsteini* Zone, Rhaetian-3, is the *M. rhaetica* Zone and Rhaetian-4 the *M. ultima* Zone, to the base of the Hettangian. Other conodont-based subdivisions of the Rhaetian have been proposed (Rigo *et al.*, 2018), but that of Krystyn (2008) is used because most Rhaetian conodont-dated magnetostratigraphies have used the zonations of Gallet et al. (2007) and Krystyn (2008).

1.b. Conflicting astrochronological durations of the Hettangian

Floating astrochronologies for the duration of the Hettangian from the Blue Lias Formation (Fm) have given conflicting interpretations. The multi-section studies of Weedon *et al.* (2018, 2019) suggested a ≥2.9 Myr Hettangian duration if using individual sections or ≥4.1 Myr when splicing together multiple sections, accounting for missing/condensed ammonite biohorizons. Tuning of the lowest observed frequency (statistically significant cycle) to the ~100 kyr short eccentricity (E2–3) astronomical period was used in these studies. Obliquity and precession cycles were also inferred, with the E2–3 cycles containing up to four limestones per cycle. This analysis was based on 2 to 4 cm spaced measurements of surface magnetic susceptibility (K_{surf}). The inferred environmental model for the connection between lithology (i.e., carbonate content) and astronomical cycles was via the degree of storminess controlling sea-floor turbulence and limestone formation (Weedon *et al.*, 2018).

https://doi.org/10.1017/S0016756825100162 Published online by Cambridge University Press

In contrast, Ruhl *et al.* (2010) and Hüsing *et al.* (2014) utilised $CaCO_3$ content, total organic carbon (TOC) and $\delta^{13}C_{org}$ (20 to 30 cm spaced sampling) to identify E2–3 cycles, based around visual interpretation of the bundling patterns of limestones and black shale beds in the St Audrie's Bay (StAB) section. The environmental interpretation was based principally on analogy with Neogene Mediterranean sapropels (Hüsing et al., 2007), which were equated to black shales in the succession and were inferred to be precession forced. In this model, sapropels/black shales matched summer insolation maxima (Hüsing et al., 2007), with bottom water anoxia corresponding to peaks in freshwater run-off (Bosmans *et al.*, 2015). These authors also observed splitting of the E2–3 band in power spectra, probably because of accumulation rate changes (Hüsing *et al.*, 2014), a feature widely inferred in the Blue Lias Fm (Weedon *et al.*, 1999). The Hüsing *et al.* (2014) c. 1.7 kyr duration estimated for the Hettangian is approximately supported by radioisotopic dates from sections in Peru (suggesting 1.93 ± 0.27 Myr for the Hettangian; Geux et al., 2012) and was additionally correlated (using magnetostratigraphy) with the astrochronology from the continental-lacustrine succession from the Hartford Basin (eastern USA). It was also linked to an astrochronology of the Pliensbachian (Xu *et al.*, 2017; Ruhl *et al.*, 2016). Although, as argued by Weedon *et al.* (2019), the Peruvian ammonite data suggest that the radioisotopically dated range may not bracket the entire Hettangian due to misidentification of some of the ammonites and potential reworking of the dated zircons.

The astrochronological assessment presented here focuses on the early Hettangian (Tilmanni Cz and Planorbis Scz), which were identified as more problematic in prior studies due to a lack of lithological bundling in the StAB section (Hüsing *et al.*, 2014). Instead, in the present account, a statistical inference approach is used that includes accumulation rate changes, a factor that was not previously considered in detail but is clearly important in limestone-marl rhythmites (Moghadan & Paul, 2000; Arzani, 2006; Westphal *et al.*, 2008; Paul *et al.*, 2008; Brett *et al.*, 2011). Unlike many astrochronologic studies, which utilise single-section/core datasets (excepting Weedon et al., 2019), a new approach is developed which utilises multi-section data to derive a composite solution with duration uncertainty.

2. Geology of the Staithes S-20 core

The Staithes S-20 borehole (location NZ 76034 18000, at the Boulby Mine, Staithes, NE Yorkshire; Fig. 1a) was completed in December 1968 and recovered the succession from the Upper Lias to the top part of the Zechstein (Woods, 1973). Depths are given here in both feet and metres since the core is labelled in (imperial) feet. The bedding dip is near zero. The core was sampled for clay mineralogy by Jeans *et al.* (1994) and Jeans (1995) and for $\delta^{34}S$ measurements from evaporites by Salisbury *et al.* (2022, 2023). Southworth (1987) also used the S-20 core as a reference section for the Middle Triassic successions of the East Midlands Shelf (Fig. 1a). Prior to the sampling for magnetostratigraphy and palynology in 1998, there had been little work on the core, which was then largely in good condition.

For the present magnetostratigraphical work, samples were taken from the succession between 357.3 m and 425.6 m (1172 ft and 1396 ft), through 17.6 m of the basal Redcar Mudstone Fm (Powell 1986; Atkinson *et al.*, 2020) of the Lias Gp; 16.6 m of the Penarth Gp; and the upper 34.1 m of the MMG (comprising the Blue Anchor Fm at 5.7 m) and the upper 28.4 m of the Branscombe Mudstone Fm (Fig. 2a). A detailed log of the sampled interval is given in the Supplementary Material (SM Fig. S3).

The Branscombe Mudstone Fm is dominated by pale red to dark-red mudstones, occasionally laminated, with anhydrite common as nodules, sometimes with chicken-wire texture or veins from 425.8 to 410.0 m (1397 ft to 1345 ft; Fig. 2a, SM Figs. S1g, S3d,e,f). Above 410.0 m (1345 ft), anhydrite occurs more typically as beds 0.07–0.6 m in thickness, with subordinate nodular anhydrite. The upper boundary of the Branscombe Mudstone Fm is at 1303.1 ft (397.18 m), at the top of the last major (~0.3 m thick) red mudstone, which overlies an anhydritic bed (SM Figs. S1f, S3d). Between 1303.1 and 1311 ft (397.18 m–399.6 m), red mudstones are interbedded with subordinate green-grey blocky mudstones in a 'variegated interval'. Such units are typical of the uppermost part of the Branscombe Mudstone Fm in sections in SW England (Mayall, 1981; Gallois, 2001, Hounslow *et al.*, 2004; Howard *et al.*, 2008). However, in S-20 the 'variegated interval' is only 2.4 m thick in contrast to the ~20 m present in sections at StAB and Haven Cliff at Seaton (Fig. 1a). The sampled part of the Branscombe Mudstone Fm can be equated to the bulk of the Keuper Anhydrite Member in offshore terminology (Fig. 1b), with the equivalent base of this unit at about 434.34 m (1425 ft) in the S-20 core. A low in $\delta^{34}S$ identified by Salisbury *et al.* (2022, fig. S2) occurs at ~417.6 m (~1370 ft).

The Blue Anchor Fm is dominated by grey to dark grey mudstones, with its top marked by 0.3 m of pyritic mudstone overlain by a bed with sandstone flasers, inferred to be at the base of the Westbury Fm (Fig. 2a, SM Fig. S1e). The Blue Anchor Fm in S-20 does not have lithological divisions corresponding to the Rydon and overlying Williton members as in sections such as StAB (Figs. 1a, b) in west Somerset (Mayall, 1981).

The base of the Westbury Formation (WFm) is uneven, with fragments of Blue Anchor Fm lithology in darker mudstones (SM Fig. S1e). The WFm is dominated by dark grey to black shaley mudstone, with a sandstone-dominated unit at 388.43–386.33 m (1274.4–1267.5 ft). Below 384.96 m (1263 ft) are common cm-scale disrupted beds of grey mudstone with sandstone clasts and bioturbated sandstone beds (Fig. 2a, SM Fig. S1c). At 387.20 m (1270.33ft; SM Fig. S1d), a bioturbated and irregular surface with meniscus burrow fills like those seen at the base of the WFm in sections in SW England (Mayall, 1981; Gallois, 2007) may mark a significant hiatus.

The base of the Cotham Member (CMbr) comprises 15 cm of silty sandstone with an irregular bed contact on the underlying mudstone (SM Fig. S1b), possibly marking a disconformity as in sections in SW England (Gallois, 2009). The remainder of this member is dark grey and grey, weakly fissile mudstones, with some reddish-grey mudstones at 381.30 m (1251 ft). The prominent desiccation surface present in the middle of the member in SW England is not present, but darker mudstones are overlain by paler mudstones, a transition which may distinguish lower and upper divisions of the member in the core (SM Fig. S3c). The overlying Langport Mbr (Fig. 2e; SM Fig. S3b) is a well-cemented grey silty-calcareous mudstone, with mm-scale sandstone flasers and lenses. It is divisible into lower and upper units, with the lower unit having more mm-scale sandy layers. The base of the Redcar Mudstone Fm (in the Lias Gp) is marked by a grey, laminated sandy-silty shale with much pyrite, possibly representing a transgressive feature (~12 cm thick; SM Fig. S1a), but with regular upper and lower contacts. The remainder of this formation consists of black to dark grey shaley mudstone and dark grey to black mudstone, with occasional laminated beds at 371.6–370.1 m (1219–1214 ft).

https://doi.org/10.1017/S0016756825100162 Published online by Cambridge University Press

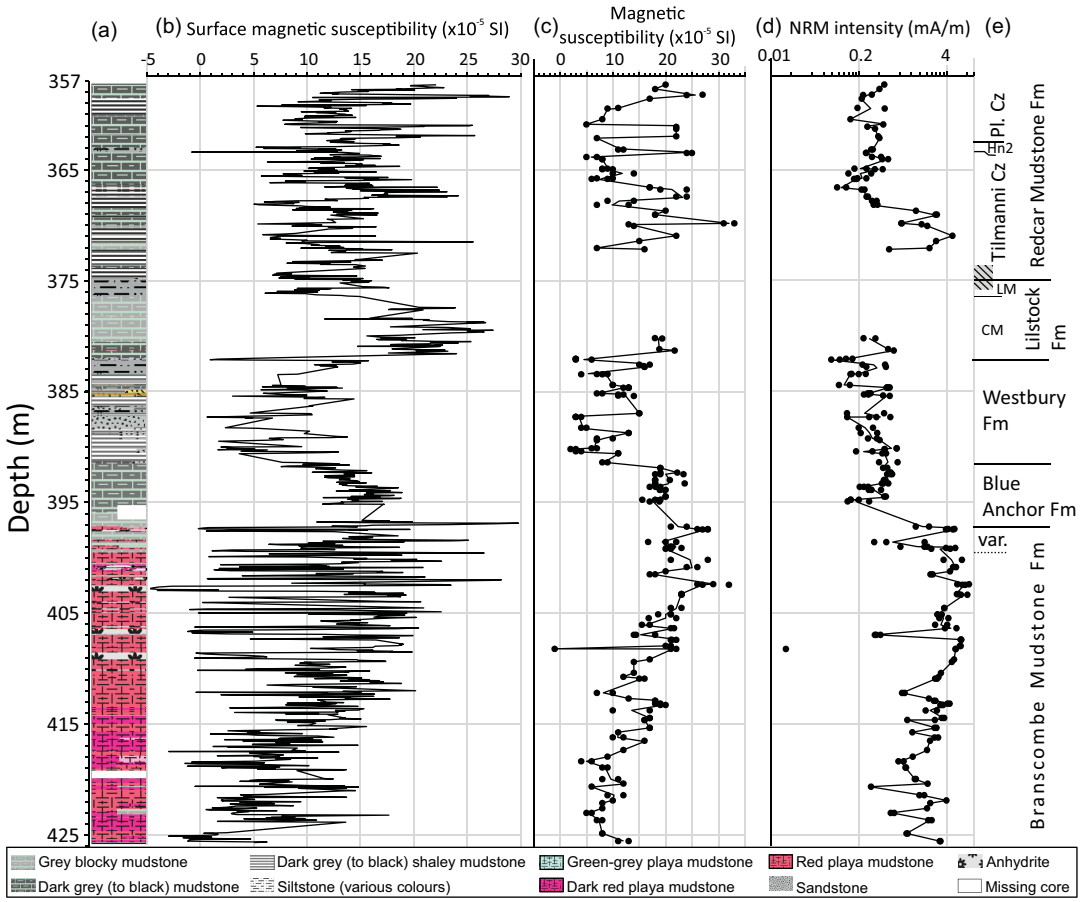

Figure 2. Summary of petromagnetic data for the Staithes S-20 core. a) Summary lithologic log (see SM Fig. S3 for details); b) surface (K_{surf}) and c) specimen volumetric magnetic susceptibility; d) natural remanent magnetisation (NRM) intensity; e) lithostratigraphy and ammonite biostratigraphy. Var.= variegated interval, CM=Cotham Member, LM= Langport Member, Cz=chronozone, Pl.=Planorbis Cz. Hatching in column (e) indicates uncertainty in the position of the base of the Hettangian.

Scattered bivalves and shell-lags progressively increase in abundance up to 364.85 m (1197 ft), above which they are very common (SM Fig. S3a).

3. Methods

3.a. Sampling for magnetostratigraphy and palynology

The S-20 core is 100 mm in diameter and non-slabbed, but at the time of sampling, some parts were fragmented (particularly in the WFm). Re-orientation of the core was attempted by first reassembling the pieces into continuous runs (Hailwood & Ding, 1995) by rotating and fitting end-pieces together to find a common reference fiducial for as many pieces as possible. This was not possible for the entire core, but 93 core runs were assembled. A few core pieces were found to be inverted, and others were misplaced in the core boxes. From the longer core runs, sample slices were dry cut with a diamond saw and prepared into 2 to 3 cm cubic palaeomagnetic specimens with a mean sample spacing of ~0.5 m for most of the core. Sampling levels and core runs are marked in SM Figure S3.

The core was sampled for palynology at 29 levels in the upper part of the MMG, the Penarth Gp and the lower part of the Lias Gp, with miospore preparations made at the British Geological Survey (BGS). The spore and pollen parent plant affinity is based on Bonis (2010), Lindström *et al.* (2017) and Gravendyk (2021). The Eco-Plant model classifications of Zhang *et al.* (2021) were used to assign humidity (EPH) and temperature (EGT) classes to each taxon, using the www.sporopollen.com database (31% of miospore taxa in the core have unclear or unknown Eco-Plant model assignment). For the three major negative carbon isotope excursions (CIE) around the Rhaetian–Hettangian boundary, the names proposed by Lindström *et al.* (2017) are used, namely Marshi CIE, Spelae CIE and top Tilmanni CIE.

3.b. Magnetic methods

Prior to any sampling, surface magnetic susceptibility (K_{surf}) was measured on the core surface, with a procedure detailed in SM Section 1. The palaeomagnetic measurement procedures follow those used by Hounslow *et al.* (2004), Hüsing *et al.* (2014), Hounslow & Gallois (2023), and Hounslow & Andrews (2024) on the same formations.

The palaeomagnetic data were analysed in a similar way to Hounslow *et al.* (2004) and Hounslow & Gallois (2023) using principal component fits with the LINEFIND software (Kent *et al.*, 1983). Directional statistics used PalaeomagTools v5.1 (Hounslow, 2023). The demagnetisation behaviour and nature of characteristic remanence were classified into either line fits (S-class behaviour) or great circle trends (T-class behaviour, fitted to a great circle plane). In each case, the degree of scatter was used for qualitative sub-division into three classes (T1 to T3 and S1 to S3), with T1 and S1 having the least scatter and being most well defined, and T3 and S3 having the most scatter and least well defined (following the

https://doi.org/10.1017/S0016756825100162 Published online by Cambridge University Press

procedures in Montgomery *et al.*, 1998; Hounslow *et al.*, 2004). A demagnetisation class of X was used for specimens which had either large directional scatter, were insufficiently demagnetised or were inferred to have no characteristic remanent magnetisation (ChRM). The inferred specimen polarity was divided into three quality categories for reverse (R, R? and R??) and normal polarity (N, N? and N??). A polarity category of U was used for specimen data in which the polarity could not be confidently assigned. The same categorisation scheme was used by Hounslow *et al.* (2004), Hounslow & Gallois (2023) and Hounslow & Andrews (2024). Magnetic mineralogy has not been investigated in detail, as it is assumed to be like that of the same formations investigated by Hounslow (1985), Briden & Daniels (1999), Hounslow *et al.* (2004), Hüsing *et al.* (2014), Hounslow & Gallois (2023) and Hounslow & Andrews (2024), data which are compared in SM Section 4.

3.c. Astrochronological methods and conceptual models of sediment accumulation rates (SAR)

Surface magnetic susceptibility (K_{surf}) from the S-20 core was used for the astrochronology, covering the Langport Mbr and Redcar Mudstone Fm (Fig. 2b). For S-20, the K_{surf} data were linearly detrended and interpolated using Hermite interpolation with third-order polynomials at the median spacing of 0.051 m (using the pchip function in R; R Core Team, 2013). The astrochronologic analysis principally uses the TimeOpt methodology (Meyers, 2014) but extends the TimeOptTemplate approach as described by Meyers (2015, 2019), which in this case specifically modelled a more complex assemblage of sediment accumulation rate (SAR) changes. TimeOpt uses a measure of overall fit of r^2_{opt}, which is a multiplication of the fits for the amplitude envelope, $r^2_{envelope}$, and the spectral power fit $r^2_{spectral}$. The astrochronological analysis used the astrochron package in R (Meyers, 2014; R Core Team, 2013). A similar analysis was applied to K_{surf} datasets from Weedon *et al.* (2018, 2019), covering the equivalent stratigraphic interval at StAB, Lavernock and Lyme Regis (Figs. 1a, 3b, c, d). These K_{surf} data are equally spaced and were not interpolated. For the early Hettangian, the fundamental secular frequencies (g_1 to g_5, precession rate k) were estimated by linear interpolation of the data in Zhou *et al.* (2022) and Meyers & Malinverno (2018) at 201 Ma (SM Fig. S2). These were converted to periods using the astrochron package, with the used periods and interpolations shown in SM Table S1. Obliquity periods at 201 Ma used those of Berger *et al.* (1992).

All previous work on cyclostratigraphy from the Blue Lias Fm uses a nominal constant SAR over ranges of ammonite chronozones. In the Redcar Mudstone Fm (and the Blue Lias), as well as longer-term changes in SAR, short-term SAR changes are probably present at the scale of the bedding (Weedon, 1986; Paul *et al.*, 2008; Brett *et al.*, 2011). We use this starting premise to evaluate probable SAR changes as a framework for a more robust astrochronological assessment, consistent between the three sections and the S-20 core. This analysis is in three stages, involving progressively more complex SAR models.

Stage 1: Baseline SAR changes (SAR_{base}) over a longer height scale than the bedding contrasts were derived from an assessment using evolutive methods of eTimeOpt (Meyers *et al.* 2001; Meyers, 2019; Omar *et al.*, 2021); the procedure is shown in Figure 4a. Evolutionary methods like eTimeOpt utilise wide data windows and are less sensitive to bedding scale variation, but SAR tracks are sensitive to the width of the data window used, so several height windows were used and a composite track produced (Fig. 4a).

Stage 2: An additional modulation was applied to the better-performing SAR_{base} models to simulate the additional effect of bedding-scale variation of SAR (referred to as SAR_{mod}; Fig. 4b). Various fractional contributions of this modulation (as measured by a value β) are added to SAR_{base}.

Stage 3: Based on placement from the ammonite biostratigraphy (Weedon *et al.*, 2018, 2019), plausible additional hiatus levels (symbolised as H) were inserted into the SAR_{base} models. This, in effect, tested various degrees of condensation at the suspected hiatus positions, a process indicated in Figure 4b (with β=0) and referred to as hiatus-testing. Using hiatus with the SAR modulation gives a composite SAR model ($SAR_{β,H}$), which includes baseline changes, hiatuses and bedding-scale SAR modulation. Two likely models of the bedding-scale SAR modulation were evaluated.

3. c.1 Modulated SAR variation models

As demonstrated by Meyers *et al.* (2001), Meyers & Sagerman (2004) and Meyers (2019), bedding-scale changes in SAR can generate spectral leakage and the generation of additional harmonics, which can confound the identification of astronomical frequencies using spectral methods (discussed at length in Hilgen *et al.*, 2015).

Modern hemipelagic carbonate–clastic rhythmites (such as those in which the siliciclastics are exclusively aeolian-derived) have their short-term accumulation rate changes controlled by clastic influx (e.g., Clemens & Prell, 1991), since carbonate production tends to be controlled by water temperature and nutrients, which can have short-term changes suppressed by the sluggishness of the oceans (Strasser, 2018). Somewhat comparable clastic-influx type models for the Blue Lias Fm were implied by Ruhl *et al.* (2010) with maximum siliciclastic input, higher TOC, more depleted $\delta^{13}C_{org}$ and larger magnetic susceptibility being observed in shale beds. This was linked to enhanced terrestrial siliciclastic input, using the Mediterranean sapropel model as an analogue (Hüsing *et al.*, 2007). The converse model of Weedon *et al.* (2018) had the same net SAR modulation effect, but the SAR minimum was interpreted as coincident with limestone beds due to winnowing of clay, with the carbonate mud being hemipelagic in origin (Weedon, 1986; Arzani, 2006) for the Blue Lias Fm, but perhaps with some shallower water-derived carbonate mud (Sheppard *et al.*, 2006). The co-varying changes in $\delta^{13}C_{org}$ and TOC indicate that, as in the geochemical tests suggested by Westphal *et al.* (2008), the lithological cyclicity is principally primary in origin, although this basic pattern is clearly modified by diagenesis (Weedon, 1986, Weedon *et al.* 2018; Moghadam & Paul, 2000; Arzani, 2006; Bottrell & Raiswell, 1989). These types of bedding-scale SAR changes are here referred to as the terrestrial-sapropel SAR model (or TS-SAR model).

The early cementation and low compaction of limestone beds is a widely agreed key observation from the Blue Lias Fm (Paul *et al.*, 2008; Weedon *et al.*, 2018). In comparison with shales and marls/shales with a greater compaction, this would increase relative SAR in the limestones (Westphal *et al.*, 2008). Irrespective of any original SAR changes, if compactional differences between limestones and marls/shales were sufficiently large, it could be that limestones have effectively larger SAR than the other lithologies. Bottrell & Raiswell (1989) have proposed a similar possibility with the marls/shales representing the lowest SAR via a linked geochemical model for limestone formation. This is here called the compaction-diagenesis model of SAR changes (or CD-SAR model).

Since K_{surf} is strongly related to carbonate content (Weedon *et al.*, 2018) and hence is a proxy for $\%CaCO_3$, it is therefore used

https://doi.org/10.1017/S0016756825100162 Published online by Cambridge University Press

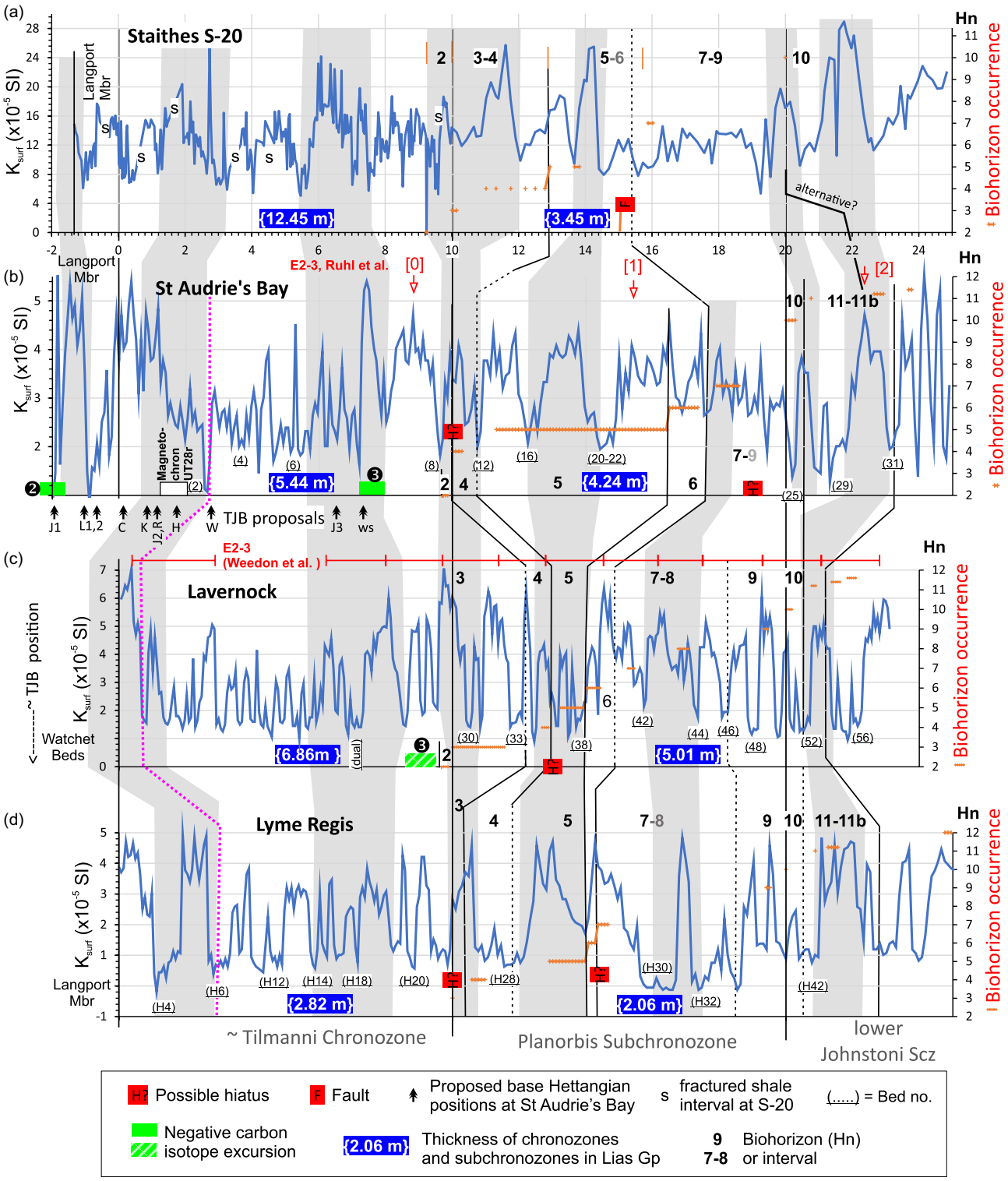

Figure 3. Surface magnetic susceptibility (K_{surf}) records from Langport Mbr and basal Lias Gp. Staithes S-20 from this work and others from Weedon *et al.* (2019). The x-axis is an arbitrary scale with the base of the Lias Gp at zero and those of the Planorbis and Johnstoni subchronozones at 10 and 20, respectively (chronozonal thickness indicated assuming base Lias Group ≅ base Jurassic). Right hand scales are the ammonite biohorizons (orange symbols, and non-underlined bold numbers). Possible hiatus levels (marked as H?) from Weedon *et al.* (2019). Black vertical lines connect biohorizon bases. The inferred short eccentricity cycle (E2–3) is marked within [ ] for St Audrie's Bay (StAB) from Ruhl *et al.* (2010) and by a red line with a tick for Lavernock (from Weedon *et al.*, 2019). Grey bands are plausible correlations of the K_{surf} changes constrained by position within the chronozones. Original error in exponent of K_{surf} corrected for the StAB, Lyme Regis and Lavernock datasets. Bed numbers from Weedon *et al.* (2019). On panel (b), the inferred positions of the base of the Hettangian correlated from the GSSP at Kuhjoch are: J1, J2, J3 (discussed by Jeram *et al.* 2021), L1, L2 = Lindström *et al.* (2021) and Lindström et al. (2017), respectively; C = Clemence *et al.* (2010) (using first occurrence of *Ps. spelae* in the New York Canyon section); K = Korte *et al.* (2019); R= Ruhl *et al.* (2020); W=Weedon *et al.* (2019), and correlation (purple dotted line); ws=Whiteside *et al.* (2010). Positions located by bed-by-bed correlation between the slightly differing logs of Weedon *et al.* (2019) and Hesselbo *et al.* (2002). The negative carbon isotope excursions (CIE) on b), c) are the positions of the Spelae ② and top Tilmanni ③ events. White bar in b) is the reverse polarity magnetozone SA5r (UT28r magnetochron). Position of the top Tilmanni $\delta^{13}C_{carb}$ CIE ③ on the Lavernock section from Korte *et al.* (2009; 2019).

https://doi.org/10.1017/S0016756825100162 Published online by Cambridge University Press

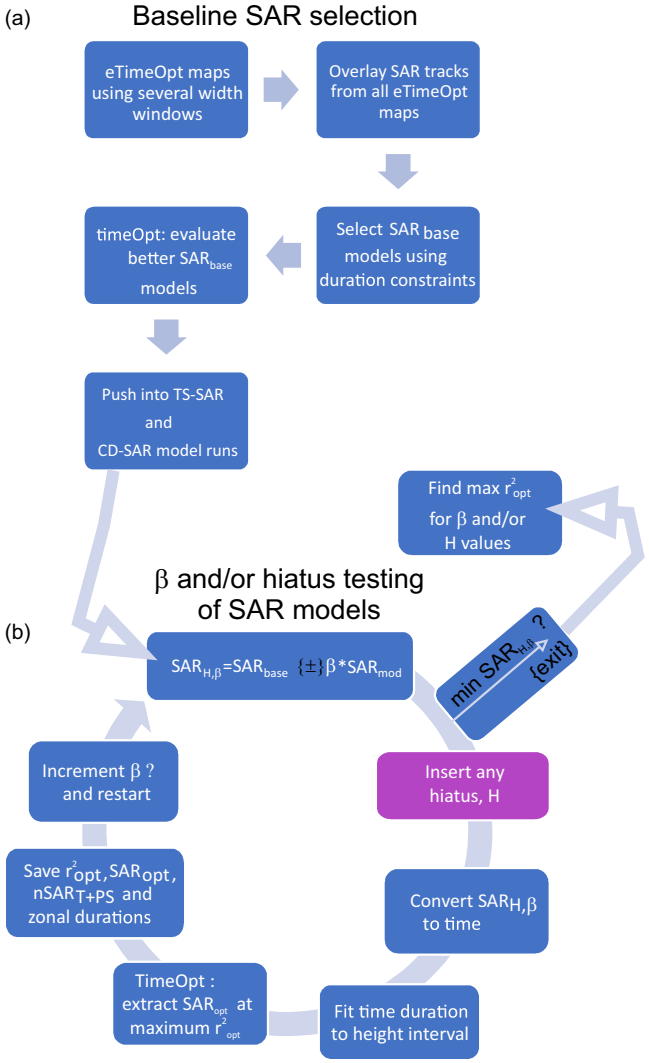

Figure 4. Outline of astrochronologic processing steps used here in developing the sediment accumulation rate (SAR) models for the sections: a) The steps principally using evolutionary TimeOpt and selecting the baseline SAR model (SAR_{base}), b) Steps in selecting the modulated SAR models, which may include hiatus levels ($SAR_{\beta,H}$). The blue steps shown are for producing the β- testing, but equally apply to variable hiatus (symbolised as H in purple step)- and β-H testing. {±} indicates β can take positive or negative values for either the TS-SAR or CD-SAR type models. The exit condition from this loop is when any element of $SAR_{\beta,H}$ is at a minimum >0.

here as a proxy for SAR_{mod}. A positive relationship between K_{surf} and SAR_{mod} corresponds to the TS-SAR model (high K_{surf} = high SAR), and a negative relationship between K_{surf} and SAR_{mod} corresponds to the CD-SAR model (high K_{surf} = low SAR). For each section, numerically, the SAR_{mod} used is the zero mean and 1σ transformed value of the K_{surf}. This transformation enables comparable inter-section modulated values of SAR_{mod} and allows it to be simply added to the more slowly changing SAR_{base}.

Formally, the composite modulated SAR (SAR_β) vector for each section (i.e., at each sampling height or depth) is based on SAR_{mod} and SAR_{base}, such that:

$$SAR_\beta = SAR_{base} + \beta^* SAR_{mod}. \quad \beta = 0 \text{ to } |SAR_\beta|, >0.0 \qquad (1)$$

($SAR_{\beta,H}$, when hiatus is added)

Varying degrees of SAR modulation are applied by differing β from 0 to the minimum possible SAR_β such that min(SAR_β) >0. For the TS-SAR model, β is positive, and for the CD-SAR model, it is negative. This procedure is referred to as ***β*-testing**. When β = 0, no SAR modulation is used, and only the baseline SAR (SAR_{base}) is applied. Any hiatus (H) can be inserted into SAR_β, giving an SAR model with both modulation and hiatus (i.e., $SAR_{\beta,H}$, Fig. 4b). When β = 0 and hiatuses are added, this procedure is referred to as **hiatus-testing**, and ***β*-H testing** when both SAR modulation and hiatus are used simultaneously. In each case, the final $SAR_{\beta,H}$ vector was converted to total duration and scaled to the height scale of the data (in meters; Fig. 4b). TimeOpt was then used to find the maximum value of r^2_{opt} for various β or H (or simultaneously β and H) at the optimum astronomical match, from which the optimum SAR vector is obtained, SAR_{opt}. Scaling of the derived duration to section/core height allows the SAR_{opt} value derived from TimeOpt to be compared with the various values of *β* and/or H. When both H and β are investigated simultaneously, these produce maps of r^2_{opt} with H and *β* (H−β maps), with the H−β position of peaks in r^2_{opt} refined by homing in on the r^2_{opt} highs identified at lower H-β resolutions. Examples of hiatus-testing are shown in SM Figs. S13 to 15, and for β - H testing in SM Figures S28 to S30. This approach is an extension of the timeOptTemplate method in the astrochron package, which simply stretches or shrinks an SAR template linearly to find the maximum r^2_{opt}. The R-scripts used are contained with the datasets (Hounslow, 2025).

These evaluation processes do not lead to unique solutions for individual sections but to several possible solutions for a range of SAR scenarios. To find optimum solutions, further constraints are applied such that **1:** any plausible fits should yield the larger r^2_{opt}, **2:** the predicted durations of the Tilmanni Cz and Planorbis Scz should be consistent between the four datasets, and **3:** the average SAR in each section should be consistent with the SAR estimated from the duration of the Tilmanni and Planorbis chronozones derived from external radioisotopic dates. External SAR constraints are detailed below. These three types of constraints therefore test the fit of the astronomical data, provide an intersection internal consistency check and an external duration constraint.

4. Results

4.a. Palynology of S-20

The palynology of the latest Triassic to earliest Jurassic succession in S-20 (studied by GW) is the most northerly such record from these successions in eastern England (see the regional review of palynology and taxonomic comments in SM Section 2). Miospore recovery from the highest beds of the Branscombe Mudstone Fm and Blue Anchor Fm in S-20 was poor in comparison with coeval sections in Somerset, but richer assemblages appear at the base of the WFm in S-20 and increase in variety upwards (Fig. 5a, SM Fig. S4). Overall, the miospore assemblages from S-20 are like those from StAB (Hounslow *et al.*, 2004), and four assemblage zones (SAB1 to 4) recognised in that succession by Bonis *et al.* (2010) can be applied in S-20 (Fig. 5a). The assemblages in these four zones have been interpreted as comprising palynofloras representing pre-extinction, extinction, recovery and post-extinction phases, respectively (Lindström, 2016; Lindström *et al.* 2017).

4. a.1. SAB1 assemblage zone (pre-extinction phase)

At StAB (Bonis *et al.*, 2010), the SAB1 Assemblage Zone (Az) extends from the base of the Williton Mbr to the top of the WFm. SAB1 associations are dominated by '*Classopollis*' (herein *Gliscopollis*) *meyeriana* and other circumpolles, *Ovalipollis*

https://doi.org/10.1017/S0016756825100162 Published online by Cambridge University Press

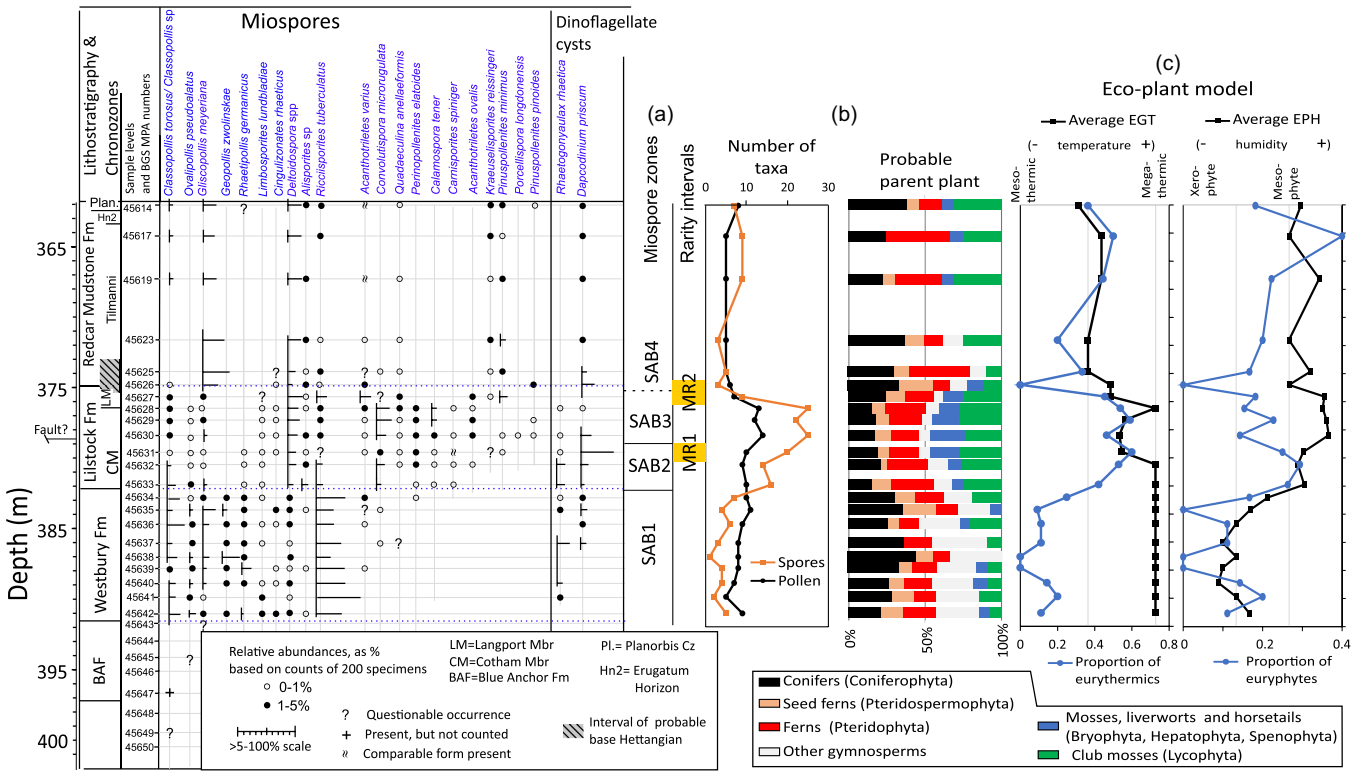

Figure 5. Summary palynomorph dataset from the Staithes S-20 core (full data in SM Fig. S4): a) selected palynomorphs from S-20 with miospore assemblage zones (SAB1 to 4) adapted from the St Audrie's Bay data of Bonis *et al.* (2010), and rarity intervals (MR1, MR2) inferred from criteria in Lindström (2021). b) relative numbers of pollen and spore taxa, and the probable parent plant groups, c) the average values for Eco-plant model EGT and EPH proxies of the pollen and spore taxa. See SM section 2 for discussion of taxonomic issues.

pseudoalatus, *Ricciisporites tuberculatus* and *Rhaetipollis germanicus*; *O. pseudoalatus* is commoner in the lower part, and small numbers of *Granuloperculatipollis rudis* and *Quadraeculina anellaeformis* occur. The last occurrence (LO) of *Enzonalasporites vigens* is ~2 m above the base of SAB1. Less diverse associations dominated by *G. rudis* and *Classpollis* sp., and with small numbers of *Leptolepidites argenteaeformis*. *O. pseudoalatus*, *Vesicaspora fuscus* and *R. germanicus*, were recorded from the Rydon Mbr, underlying the Williton Mbr at StAB (Warrington & Whittaker 1984; Warrington *in* Hounslow *et al.* 2004).

In S-20 associations from the WFm (Figs. 5a, SM S4) are like those in SAB1 at StAB, but with high numbers of *R. tuberculatus*, *G. meyeriana* and other circumpolles; *O. pseudoalatus*, *Geopollis zwolinskae*, *R. germanicus* and *Deltoidospora* spp. with each typically comprises at least 5% of these associations; *G. zwolinskae* was only recorded in SAB1 at S-20. Small numbers of *Zebrasporites laevigatus*, *Vesicaspora fuscus*, *Limbosporites lundbladiae*, *Microreticulatisporites fuscus* and *Cingulizonates rhaeticus* are present, and *Lunatisporites rhaeticus*, *Acanthotriletes varius*, *G. rudis*, *Convolutispora microrugulata* and *Semiretisporites gothae* appear progressively upwards in the section; *G. rudis* was not noted above this Az.

4. a.2. SAB2 assemblage zone (extinction phase)

At StAB (Bonis *et al.*, 2010), the SAB2 Az extends from the base of the CMbr into the upper part of that member, below the hiatus/ desiccation surface. The base of this Az is marked by an increase in the numbers of a wide range of spores and in the abundance of *Vitreisporites* spp. and *Tsugaepollenites pseudomassulae*. The LOs of *Ovalipollis pseudoalatus*, *Rhaetipollis germanicus* and *Lunatisporites rhaeticus* are at the top of this Az. From closely spaced samples, Bonis *et al.* (2010) recognised two peaks in spore abundance in SAB2. Components of the lower peak include *Porcellispora longdonensis*, '*Heliosporites*' (herein *Kraeuselisporites*) *reissingeri*, *Deltoidospora* spp., *Concavisporites* spp., *Carnisporites anteriscus* and *Todisporites* spp.; the main components of the upper peak are *Calamospora tener*, *Deltoidspora* spp. and the bryophyte spore *P. longdonensis*, the acme of which is in the upper peak.

In S-20, the miospore association from sample MPA 45633 is interpreted as the lowest in the SAB2 Az. This sample (Figs. 5a, SM S4) is likewise dominated by circumpolles and *R. tuberculatus* but fewer *O. pseudoalatus* and *R. germanicus* are present. Other features in higher samples in SAB2 are the absence of *G. rudis*, increases in the numbers of *Deltoidospora* spp., *Convolutispora microrugulata* and *Perinopollenites elatoides*, and the incoming of small numbers of *Calamospora tener* and definite specimens of *Zebrasporites interscriptus* and *Kyrtomisporis* spp., and species of other spore genera including *Carnisporites* and *Densosporites*. The mass rarity interval MR1 of Lindström (2021) is probably present in MPA 45631, with a rarity of *Classopollis* sp., the LO of *R. germanicus* and marked decline in *R. tuberculatus* (Fig. 5a). The occurrence of MR1 in the SAB2 Az is also a feature at StAB (Lindström, 2021).

4. a.3. SAB3 assemblage zone (recovery phase)

At StAB, the succeeding SAB3 Az extends from the upper part of the CMbr to the top of the Langport Mbr. In this Az, there are wide variations in the relative abundances of circumpolles and a wide range of spore taxa present (Bonis *et al.*, 2010). Two peaks in spore

https://doi.org/10.1017/S0016756825100162 Published online by Cambridge University Press

abundance were recognised with the lower peak dominated by *Acanthotriletes varius*, *Concavisporites* spp., *Conbaculatisporites* spp. *Deltoidospora* spp., *Kraeuselisporites reissingeri* and *Trachysporites fuscus*. The upper peak consists mainly of *Polypodiisporites polymicroforatus*, *Calamospora tener*, *Porcellispora longdonensis*, *Deltoidospora* spp. and *Todisporites* spp. Notable features of this Az are the absence of *Tsugaepollenites pseudomassulae* and the very high abundance of *K. reissingeri* in the upper part of the lower spore peak, ~1.0 m above the base of the Az. The Spelae CIE also occurs in the lower part of SAB3 at StAB.

Locating a comparable position for the SAB2 /SAB3 boundary in S-20 is difficult because of the smaller number of sample levels from S-20. Differences also probably arise from the hiatus/desiccation surface at StAB between the lower and upper CMbr (Gallois, 2009) and/or because of a fault at 1243.5 ft (378.66 m) in S-20, which may have cut out part of the CMbr. In S-20 (Figs. 5a, SM S4), a change from associations with similar proportions of pollen and spores to one dominated by circumpolles and with fewer spores is probably the clearest way to define this boundary and is here interpreted as between samples MPA 45631 and 45630. The LO of *R. germanicus* is in MPA 45631, but those of *Ovalipollis pseudoalatus* and *Lunatisporites rhaeticus*, which also occur at the Az boundary at StSB, occur higher in the S-20 core. Of the taxa which are relatively common in SAB2 at S-20 but are scarce or absent in SAB3 at StAB, lower numbers of *R. tuberculatus* occur above MPA 45631, but those of *C. tener* increase. A greater number of taxa (SM Fig. S4) are recorded above MPA 45631 than at the base of SAB3 at StAB. Of these, *Perinosporites thuringiacus* and *Cornutisporites rugulatus* appear in MPA 45630, and *Stereisporites perforatus*, *Neochomotriletes triangularis* and *C. seebergensis*? appear slightly higher. Taxa recorded both below and above the SAB2/3 boundary in S-20, but not from StAB by *Bonis et al.* (2010), include *Limbosporites lundbladiae*, *Cingulizontes rhaeticus*, *Chas matosporites magnolioides*, *Convolutispora microrugulata*, *Semire tisporis gothae*, *Contignisporites problematicus*, *Triancoraesporites ancorae*, *Annulispora folliculosa* and species of the genera *Zebrasporites*, *Kyrtomisporis* and *Stereisporites*; but several of these taxa were recorded in the StAB section by Warrington (*in* Hounslow *et al.*, 2004, fig. 5).

4. a.4. SAB4 assemblage zone (post extinction)

In the StAB section (Bonis *et al.*, 2010), the SAB4 Az extends from the top of the Lilstock Fm upwards for ~14 m into the Hettangian of the Blue Lias Fm. Miospore associations in this Az are dominated by *G. meyeriana*, with *K. reissingeri* a minor but prominent component at several levels. *Carnisporites* spp. and *R. tuberculatus* only occur in the lower ~4 m of the Az and *Cerebropollenites thiergartii* first appears ~4 m above the base of SAB4. Also recorded were scattered occurrences of *Porcellispora longdonensis*, *Quadraeculina annellaeformis*, *Tsugaepollenites pseudomassulae*, *Chasmatosporites* spp., *Vesicaspora fuscus* and other bisaccates, and *Deltoidospora* spp. and other trilete spores. At StAB, the main change between SAB3 and SAB4 is from a relatively varied association to a comparatively impoverished one.

In S-20, the miospore association from sample MPA 45626 is interpreted as the lowest in the SAB4 Az. At this level in S-20, there is a change from a relatively varied association to a comparatively impoverished one (Figs. 5a, SM S4). In the SAB4, Az *G. meyeriana* is almost the only circumpolles present and dominates an association that includes small numbers of *Deltoidospora* spp., *Alisporites* sp., *Acanthotriletes varius* and *Pinuspollenites pinoides*, and a few specimens of *Cingulizonates rhaeticus*, *R. tuberculatus* and *Vitreisporites pallidus*. The mass rarity interval MR2 of Lindström (2021) occurs in the Langport Mbr in S-20 and is marked by the LO of *Limbosporites lundbladiae*, the absence of *Semiretisporites gothae, Perinopollenites elatoides, Lunatisporites rhaeticus* and a virtual loss of *Convolutispora microrugulata*, and the recovery of *Gliscopollis meyeriana*. Lindström (2021) placed MR2 in the upper part of the CMbr at StAB, marked by rarity in *Lunatisporites rhaeticus*, *Perinopollenites elatoides*, *Polypodiisporites polymicroforatus* and *Ricciisporites tuberculatus*. This difference perhaps relates to diachronous variation in the expression of the MR2 event, or the more widely spaced sampling intervals in the Lilstock Fm of S-20 inadequately display MR2.

4. a.5. Dinoflagellate cysts, acritarchs, prasinophyte algae

At StAB, the dinoflagellate cysts *Rhaetogonyaulax rhaetica* and *Dapcodinium priscum* appear in the Williton Mbr at the top of the Blue Anchor Fm and dominate aquatic palynomorph associations from the WFm and CMbr, with abundance peaks of *R. rhaetica* alternating with those of *D. priscum* (Bonis *et al.*, 2010). These alternations may reflect changes from more fully marine environments, with *R. rhaetica*, to more marginal ones, with *D. priscum* (Poulsen, 1996, p. 45). Courtinat & Piriou (2002) interpreted *D. priscum* as a euryhaline form that occupied a range of ecological settings in low to high energy levels in nearshore and restricted marine environments and *R. rhaetica* as indicative of more open, low-energy marine conditions with greater water depth. Other dinoflagellate cysts were present in very small numbers in these associations (Bonis *et al.*, 2010) and include *Heibergella asymmetrica* in the Williton Mbr and the middle of the WFm, *Beaumontella langii* at similar levels, *Cleistosphaeridium mojsisovicsii* at the base of the WFm and *Suessia swabiana* throughout that formation and in the CMbr. Bonis *et al.* (2010) did not record *R. rhaetica* above the CMbr, but it occurs in very low numbers in the higher part of the Lilstock Fm and the lowest ~10 m of the Lias (Warrington *in* Hounslow *et al.*, 2004). In the upper part of the Lilstock Fm, dinoflagellate-dominated associations are replaced by ones dominated by acritarchs, predominantly *Micrhystridium* spp., and prasinophytes, mainly leiospheres; below that level, *Micrhystridium* occurs infrequently in the Williton Mbr and WFm, but leiospheres are common in the former and the lower half of the latter. Samples MPA45619 and MPA45617 have a higher abundance of acritarchs (SM Fig. S4) and probably relate to the bloom of prasinophytes and acritarchs similarly located in the upper part of the Tilmanni Cz at StAB (Van de Schootbrugge et al., 2007).

The record of aquatic palynomorphs in S-20 (Figs. 5a, SM S4) is broadly comparable with that from StAB, although without leiospheres. The dinoflagellate *R. rhaetica* is commonest in the lower half of the WFm and the lower CMbr and occurs in very small numbers in the higher part of the Lilstock Fm but was not recorded higher; *Dapcodinium priscum* was recorded from the middle of the WFm to the lower part of the Planorbis Cz in the Redcar Mudstone Fm, with peaks in the middle of the CMbr and around the boundary between the Lilstock and Redcar Mudstone formations.

4. a.6. Environmental assessment

Mass occurrences of the dinoflagellate cyst *R. rhaetica* are probably indicators of maximum flooding surfaces (Lindström & Erlström, 2006; Gravendyck *et al.*, 2020). An earlier acme event is the '*Lunnomidinium* interval' (Lindström & Erlström, 2006), in which *Lunnomidinium scaniense* is associated with a few *Beaumontella*

https://doi.org/10.1017/S0016756825100162 Published online by Cambridge University Press

caminuspina and *Suessia swabiana* in the lower parts of the Contorta Beds (Lindström & Erlström, 2006). This event may be present in the middle of the WFm in S-20, where a possible *B. caminuspina* occurs in sample MPA 45639 (SM Fig. S4). A more widely recognised flooding event (MFS7, Rh2) occurs around the SAB1–SAB2 boundary, prior to the Spelae CIE (Lindström *et al.*, 2017; Barth *et al.*, 2018). This is within the acme of *Polypodiisporites polymicroforatus* corresponding to the common occurrences of *C. microrugulata* above the last common occurrence of *R. rhaetica* in sample MPA45632 in S-20 (Fig. 5a).

The abundance in the diversity of spores seen in S-20 (Fig. 5a, SM S4) is a widely observed feature of the extinction and immediate recovery interval at many other locations (Orbell, 1973; Van de Schootbrugge *et al.*, 2009; Bos *et al.*, 2023), and a similar response is apparent in the probable parent plants, with increases in mosses, liverworts, horsetails, ferns and club mosses, and proportional reductions of gymnosperms and conifers (Fig. 5b). Using the Eco-plant model data of Zhang *et al.* (2021), the change from SAB1 to SAB3 shows an increase in palaeoclimatic humidity (EPH proxy) which begins in the upper part of SAB1 and is largely achieved by the middle of SAB2 (Fig. 5c). From the analysis of miospore data from StAB, Bonis & Kürschner (2012) inferred an increase in humidity starting near the base of the CMbr with stabilisation by the start of the Lias Gp; a similar trend is shown by the EPH proxy for S-20.

From the upper part of the SAB2 Az, a progressive decline in temperature is apparent from the EGT proxy (Fig. 5c). Eurythermic parent plants (those tolerant to a wide range of temperatures) show a major proportional increase at a rate like that of the change in the EPH proxy. Euryphytes (tolerant to a wide range in humidity) show an erratic proportional increase over the same interval (Fig. 5c). These changes are interpreted as related to the habitat disturbance and ecosystem stress associated with the initial phase of the end-Triassic extinction.

4.b. Ammonites in Staithes S-20 and the base of the Jurassic

The base of the Hettangian Stage is formally defined at the ratified GSSP at Kuhjoch in the Karwendel Mountains (Austria) based on the first occurrence of the ammonite *Psiloceras spelae* Guex *tirolicum* Hillebrandt & Krystn (Hillebrandt & Krystyn 2009, Hillebrandt *et al.* 2013) – a species closely related to *Ps. tilmanni* Lange from South America – hence the use of a Tilmanni Cz at the base of the Jurassic System in both South America and Europe (Page, 2010; Weedon *et al.*, 2018, 2019, Boomer *et al.*, 2021; Kment, 2021; Hesselbo *et al.* 2023; SM Section 3). In the absence of any records of *Ps. spelae* elsewhere in Europe, alternative means of correlating the base of the Jurassic System (TJB) from the GSSP are necessary, principally using carbon isotope curves (Hillebrandt *et al.*, 2013; Korte *et al.* 2019; Ruhl *et al.* 2020), or Hg chemostratigraphy (Yager *et al.* 2021), or using a combination of organic carbon isotopes and palynological changes (Lindström *et al.*, 2017; Boomer *et al.*, 2021). Using these correlation methods, a number of proposed positions for the base of the Hettangian have been suggested at StAB (black arrows, Fig. 3b). The positions in the Langport Mbr principally relate to using palynological data in addition to isotopic changes, whereas the TJB inferred in the basal Lias Gp principally used $\delta^{13}C_{org}$ isotope data. Weedon *et al.* (2019) also transferred the inferred position at StAB to other UK sections using astronomical cycles (dotted purple line, Figs. 3b, c, d). At Lavernock, the base of the Jurassic is probably at or near the base of the 'Watchet Beds' of the Langport Mbr based on carbon isotopes and magnetic polarity data (Korte et al., 2009; 2019; Hounslow & Andrews, 2024), close to an underlying 'new' species of the ammonite *Neophyllites* (Hodges, 2021), a species which could also be of latest Rhaetian age (Page in Hesselbo *et al.* 2023, p.18). The standard ammonite zonal framework follows Page (2010), including the latest available sequence of high-resolution bio-horizons (coded as Hn), as used by Weedon et al. (2018, 2019), and summarised in SM Section 3.

The lowest ammonites present in the Staithes borehole correspond to *Psiloceras erugatum* (Phillips 1829), which occurs between 1192.17 ft and 1192.25 ft (363.37–363.4 m; Fig. 6c), indicating the upper part of the Tilmanni Cz (Hn2), included within calcareous nodules. *Ps. erugatum* (Figs. 6a, b) is the lowest confirmed Jurassic ammonite recorded across the British and Irish islands and, as well as the biohorizon, can be taken to mark the base of an Erugatum *Horizon* (i.e., sub-subchronozone; Page, 2017). The record in S-20 is particularly important, as it is the first time that the species has been recorded in situ close to its type locality in nearby Robin Hoods Bay, where the species has been collected since the early 19th century from loose calcareous concretions on the beach (Howarth 1962, 2022; Fig. 6d). The borehole record confirms that the species is present *in situ* in the Cleveland Basin in typical preservation and places the beach concretions at a defined level in the Redcar Mudstone Fm. The species is characterised by a nucleus with small bead-like nodes, hence linking it closely to *Ps.* grp *tilmanni,* followed by middle and outer whorls which range from plicate to smooth (Bloos & Page 2000; Fig. 6d). The holotype of the species (NHM 37981) has been refigured several times, including by Howarth (1962, pl.14, figs. 2a, b).

At 1192.04 ft (363.33 m), a larger (68 mm) essentially smooth *Psiloceras* with a typical suture suggests a continuation of the *erugatum* biohorizon (Hn2). At 1189.08 ft (362.43 m), a small evolute cf. *Neophyllites* (Fig. 6e) indicates the base of the Planorbis Chronozone and Subchronozone and probably Hn3 (with *Ne. imitans* Lange) with evolute, smooth forms from 1186.04 ft to 1188.0 ft (361.50–362.10 m), suggesting *Ne. antecedens* Lange of Hn4 (Fig. 6f). Relatively, involute *Ps.* cf. *planorbis* indicates the base of *planorbis* α Biohorizon (Hn5) with large (d = 68 mm) and more evolute forms from 1183.83 ft [360.12 m], indicating the *planorbis* β Biohorizon (Hn6). As in West Somerset (Bloos & Page 2000), rare *Neophyllites* persists into the lower Planorbis Scz in S-20, at least as far as Hn5, where two specimens with characteristic spiral grooves are present at 1185.79 ft (361.43 m). *Ps. plicatulum* at 1182.5 ft (360.43 m) indicates the base of the *plicatulum* biohorizon (Hn7).

No further age diagnostic specimens have been noted below the first record of *Caloceras* of the overlying Johnstoni Scz at 1177.83 ft (359.00 m). The latter, however, does not have the typical blunt ribbing of basal Johnstoni Scz *Ca. aries* of Hn10, as its ribs are relatively sharp and hence could represent a slightly younger species, for instance, of Hn11b–11d.

The nearest comparable record of the earliest part of the Hettangian is from the Felixkirk borehole (Ivimey-Cook & Powell, 1991; Fig. 1a), which has an ammonite record like S-20. Ivimey-Cook & Powell (1991) did not distinguish a Langport Mb at Felixkirk, although in a more detailed assessment Beith *et al.* (2023) considered the lowest 1.7 m of the Calcareous Shales Mbr as the Langport equivalent, with the Spelae CIE in the lower half of this member. As *Ps. erugatum* and *Neophyllites* were not distinguished at Felixkirk, the lowest recorded ammonites (at 11.89 m above the base of the Calcareous Shales Mbr, using the revised base of Beith et al. 2023) could either be end Tilmanni Cz or lower Planorbis Scz.

https://doi.org/10.1017/S0016756825100162 Published online by Cambridge University Press

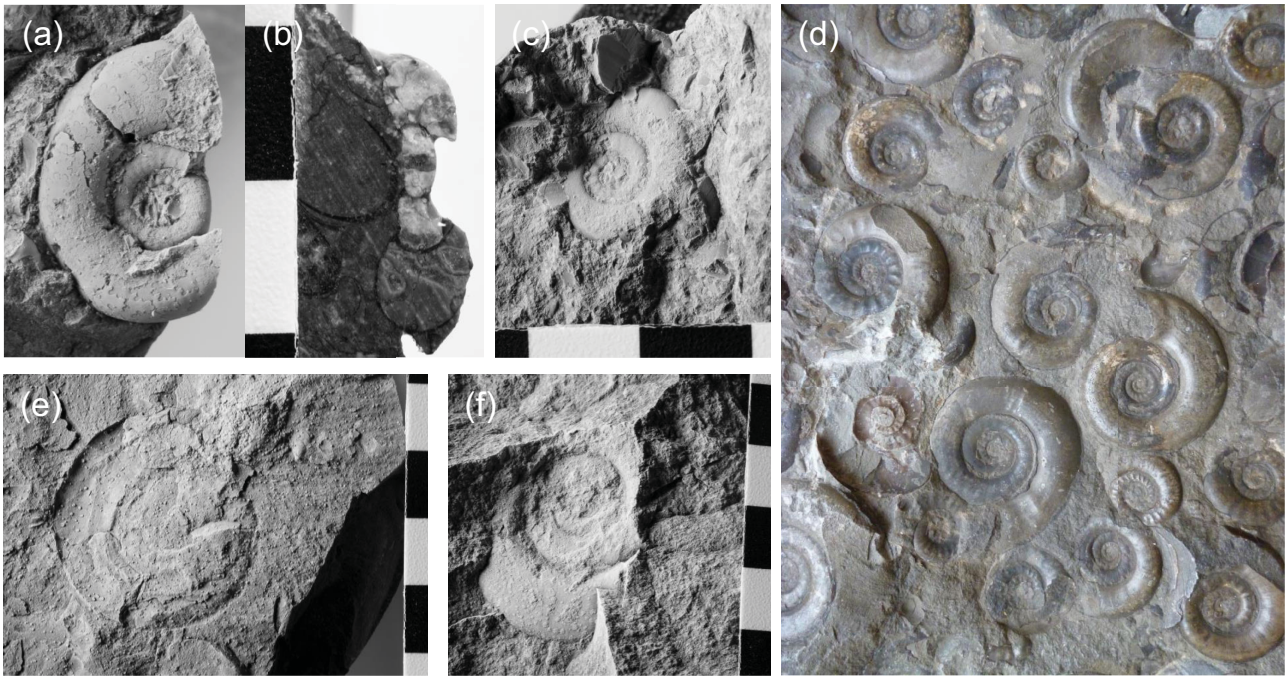

Figure 6. Earliest Jurassic ammonites from the northern Cleveland Basin (in following P*nnn*= BGS photo assess number): *Psiloceras erugatum* (Phillips): A, B- GSM BKK 3156 (P1057099, P1057097), C- GSM 3157 (Staithes S-20 at 1192.2 ft, 363.38 m, P1057104), D- NHM37881, "Robin Hoods Bay, Yorkshire", ex W. Bean coll.1859 (detail of typical concretion recovered ex-situ) (note node-like tubercles on nuclei and variable expression of ribbing on middle and outer whorls). E- cf. *Neophyllites* sp (GSM 3154, P1057092), Staithes S-20 at 1181.17 ft, 360.02 m). F- *Neophyllites* sp. cf. *antecedens* Lange (GSM 3151, P1057084), Staithes S-20 at 1179.00 ft, 359.35 – note relatively steep umbilical wall when compared to typical *Psiloceras* spp. (scale bar with 1 cm intervals for A-C, E, F; field of view for D. 70x120 mm). A-C, E, F by S. Harris BGS, D by KNP. *British Geological Survey materials © UKRI 2024; containing public sector information licensed under the Open Government Licence v3.0.*

Ps. plicatulum at around 4.9 m higher (+16.8m) would at least confirm the upper part of the latter (i.e., Hn7–9), with the highest recorded *Psiloceras* at +17.6 m and *Caloceras* spp. from +21.7m to around +22.4m, indicating the Johnstoni Scz. Similarity to Felixkirk is also in the thickness of the Calcareous Shales Mbr below the first occurrence of ammonites, i.e., 11.9 m and 12.45 m above the base of the Lias Group in the Felixkirk borehole and S-20, respectively. However, the Planorbis Scz is thinner at S-20 than Felixkirk (3.5 m compared to 5.7 m). If the succession in S-20 is comparable to that at Felixkirk, the Spelae CIE should be around the lower part of the Langport Mbr in the core (Beith *et al.*, 2023), allowing a reasonably precise correlation to StAB (Fig. 3a,b).

4.c. Magnetic and palaeomagnetic results

The variability in K_{surf} in the Branscombe Mudstone Fm is largely related to anhydrite content (Fig. 2b). In the overlying formations, variation is likely inversely related to carbonate content, with a variable content of paramagnetic minerals probably in the clay or silt fraction. This is similar to conclusions inferred from other studies of these units (Hounslow, 1985; Deconinck *et al.*, 2003; Hounslow *et al.*, 2004; Hüsing *et al.*, 2014; Weedon *et al.*, 2018), discussed at length in SM section 4. The remanence-carrying mineralogy is similar to these formations investigated in SW Britain (see SM Section 4; Fig. S5).

4. c.1. Magnetisation components

The magnetisations comprise three components. Firstly, a low stability component (LTC), which was typically removed by 100–150°C, occasionally persisting up to 200°C or 300°C; 88% of specimens contained this component. This was often shallow to intermediate in inclination, with 88% showing downward-directed and 12% upward-directed components (SM Fig. S6a). The origin of this component is unclear, but it may represent a short-term viscous component, one acquired during core storage since 1968, or perhaps a combination of this and higher stability components. The large directional scatter of the LTC precludes anything useful being inferred from it (SM Fig. S6b).

Secondly, an intermediate stability component (MTC; 74% of specimens), which largely has a steep inclination and is down-directed (mean inclination +63°, $\alpha_{95} = 2.2°$, k = 17.8; mean using the likelihood function of Enkin & Watson, 1996), although 6.6% of these specimens had steep up-directed components (SM Fig. S6c; example demagnetisation diagrams in SM Fig. S8). The MTC typically displays a marked directional break with the LTC on Zijderveld plots (see SM Fig. S8). The MTC is often a major part of the natural remanent magnetisation intensity. The stability range of the MTC commonly started from 150°C or 100°C (occasionally ranging to 350°C, SM Fig. S7a). The upper stability range was most commonly up to 400 to 450°C during thermal demagnetisation, although this was quite variable, from 200 to 650°C in some specimens (SM Fig. S7a). For specimens using a combined demagnetisation scheme, the upper stability range was typically 10–30 mT but was up to 80 mT in rare some. In 4.4% of specimens, the MTC dominated, and no ChRM was detected. This component is interpreted as a magnetisation acquired during the Brunhes Chron. A similar Brunhes age overprint has been identified in coeval units in southern Britain (Briden & Daniels, 1999; Hounslow *et al.*, 2004; Hüsing *et al.*, 2014; Hounslow & Gallois, 2023).

Thirdly, the highest stability characteristic remanence (ChRM) was detected in 89.2% of demagnetised specimens. Of these, 81% had S-class behaviour and 19% had T-class behaviour (Fig. 7b). The ChRM has both positive and negative inclinations (Fig. 8c,d).

https://doi.org/10.1017/S0016756825100162 Published online by Cambridge University Press

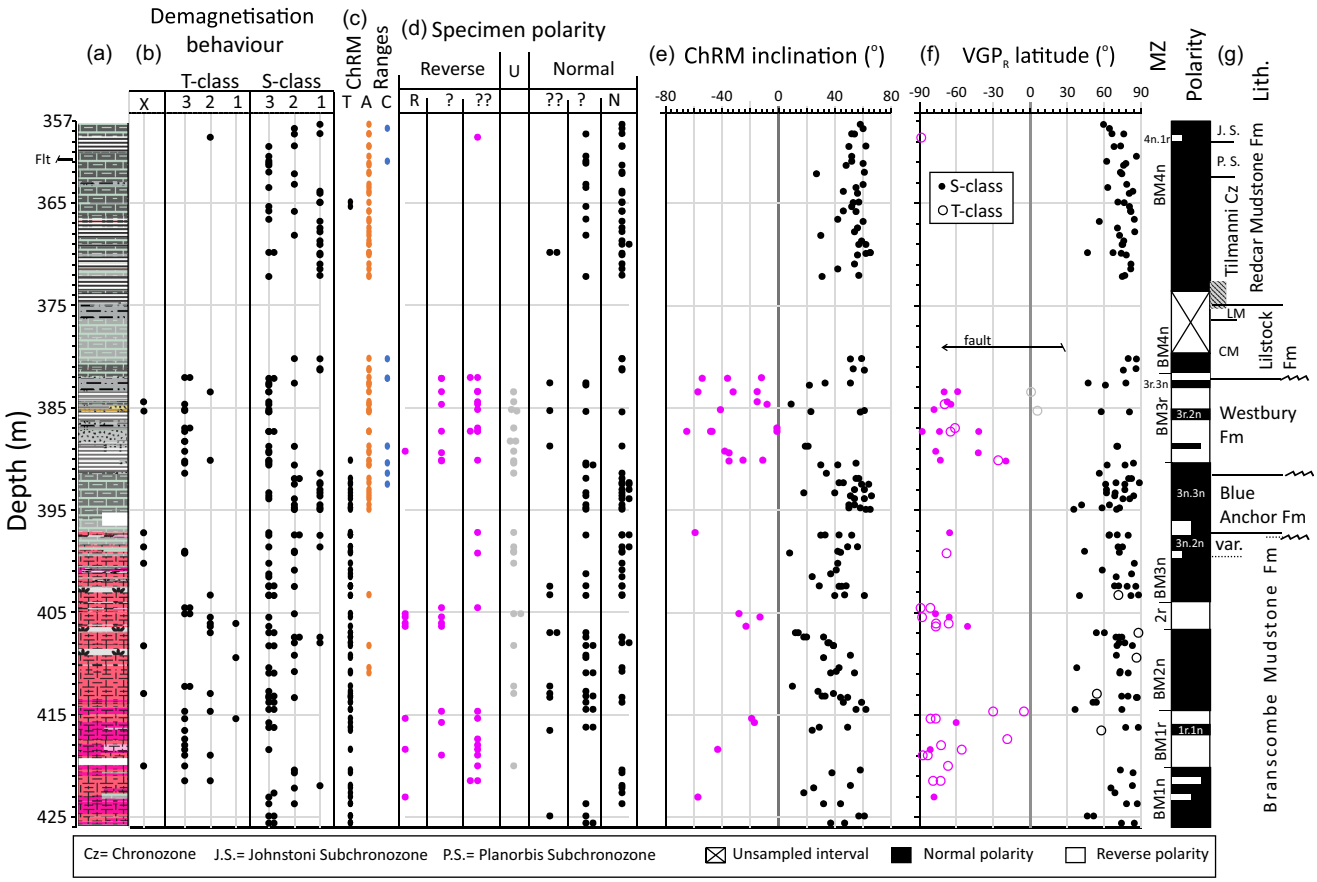

Figure 7. Summary magnetostratigraphic data for the Staithes S-20 core. a) Simplified sedimentary log (SM Fig. S3 for details, key in Fig. 2). b) Demagnetisation behaviour classification of specimen data. c) Characteristic remanent magnetisation (ChRM) isolation method during demagnetisation (T=thermal, A= alternating field, C= combined). d) Specimen polarity classification. e) Specimen ChRM inclination. f) Specimen virtual geomagnetic pole latitude (VGP_R) with respect to the mean poles for the Branscombe Mudstone Formation and the Penarth and Lias groups (core re-oriented using joint mean-run rotation angle). g) Section polarity, lithostratigraphy (Lith.) and biostratigraphy. MZ= labels of magnetozone couplets (BM = Boulby Mine, the location of the core). LM= Langport Member, CM= Cotham Member, var.=variegated unit. Hatching in column (g) represents the interval of probable base Hettangian.

Converted to positive, the mean inclination of all data from S-class specimens is 47.7° ($\alpha_{95} = 2.4°$, k = 15.8, n = 135; method of Enkin & Watson, 1996). The ChRM was predominantly isolated by thermal demagnetisation (SM Fig. S7b,c) in the Branscombe Mudstone Fm and by AF demagnetisation in the Penarth and Lias groups. The Blue Anchor Fm specimens possess a mix of isolation methods (Fig. 7c). A few ChRM's were isolated by overlapping thermal and AF demagnetisation ranges. Using only thermal demagnetisation, the starting range of this component was variable but largely between 300°C and 600°C, with a few specimens outside this (SM Fig. S7b). The S-class line fits were predominantly through the origin. For those in which the ChRM was isolated by AF demagnetisation (Fig. 7c), the start AF ranges were 10–70 mT, with the end ranges largely through the origin and others mostly ending in the range 50 to 80 mT (SM Fig. S7b). For some specimens the demagnetisation noise and thermal alteration largely precluded origin fits. The ChRM is interpreted as a Late Triassic–Early Jurassic magnetisation.

For the 6.6% of specimens with a steep up-directed MTC component, this was assumed to be the result of inverted core runs. These occurred in three runs (run codes ST6, ST7 and ST36; SM Fig. 3f, d). Within ST7, the inverted segments were adjacent in the middle of the run, indicating core-segment re-assembly was imperfect for this run. For runs ST6 and ST36, the whole runs were inverted. The magnetisation directions from these inverted segments and runs were rotated by 180° about the horizontal plane.

To reorient the runs, the average declination of the MTC within each run was used to determine a rotation angle to bring the average declination to 0°. Applying this rotation angle to reorient the ChRM directions gives an estimate of the directional distribution of the ChRM directions (Fig. 8a). This reorientation approximately produces directions like the expected Rhaetian–Hettangian directions, supporting the inferences made about the origins of the MTC and ChRM directions. However, ten of the 49 core runs sampled could not be reoriented using the MTC.

Similarly, if the mean declinations of the ChRM in the runs are used to reorient the MTC, it gives a directional distribution (Fig. 8b) similar to that in other Brunhes-age overprints observed in these formations (Hüsing *et al.*, 2014; Hounslow & Gallois, 2023; Hounslow & Andrews, 2024). The ChRM mean declinations expected for S-20 are 037° and 019° for the upper Mercia Mudstone Fm and Penarth/Lias groups, respectively (using palaeopole data from Hounslow *et al.*, 2004, Hüsing *et al.*, 2014 and Hounslow & Gallois, 2023). The resulting Fisher mean inclination of the reoriented MTC is 68.7° ($\alpha_{95} = 4.4°$), which is close to the expected Brunhes-age inclination of 70.4° (Fig. 8b).

https://doi.org/10.1017/S0016756825100162 Published online by Cambridge University Press

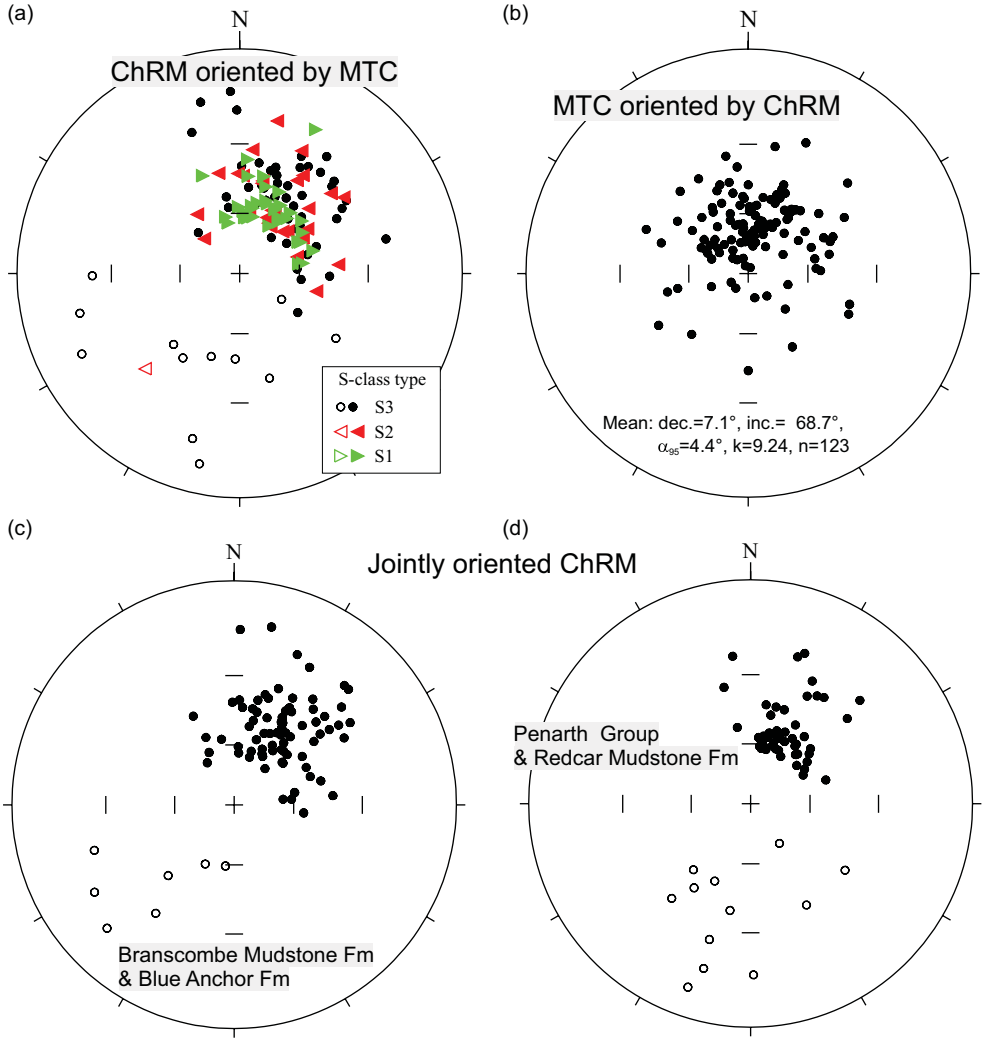

Normal polarity: dec.=032.5°, inc.= 47.3°, α_{95}=4.4°, k=14.82, n= 76
Reverse polarity: dec.=225.0°, inc.= -35.5°, α_{95}=19.0°, k=11.10, n= 7
All: dec.= 33.7°, inc.= 46.4°, α_{95}=4.3°, k=14.13, n= 83
Reversal test: Rc, γ_{obs}=15°, γ_{crit}=15.3°

Normal polarity: dec.=026.3°, inc.=50.5°, α_{95}=4.3°, k=23.01, n=50
Reverse polarity: dec.=189.3°, inc.=-37.0°, α_{95}=16.2°, k=8.15, n=12
All: dec.=22.6°, inc.=48.3°, α_{95}=4.7°, k=15.58, n=62
Reversal test: Ro, γ_{obs}=18.2°, γ_{crit}=22.2°

Figure 8. Component directional data when re-oriented: a) Specimen ChRM directions re-oriented by the mean MT component (inferred Brunhes-age) in each run; b) MT-component (MTC) re-oriented by the mean-run ChRM declination; c) and d) specimen ChRM directions for formational groupings, re-oriented by the combined MTC and ChRM declinations for each run. Fisher mean directions shown for b), c) and d), and the reversal test for c) and d), with classification, observed (γ_{obs}) and critical (γ_{crit}) angle of divergence.

4. c.2. Defining the magnetostratigraphy:

In order to utilise the directional information from the T-class specimen ChRM's and determine an estimate of VGP latitude (VGP_R) for each specimen, the core runs were reoriented by using both the MTC and ChRM declinations (i.e., averaging the rotation angles of both sets in each run). These 'jointly reoriented' ChRM data are shown in Figure 8c and d. Whilst this procedure introduces dependence on externally derived palaeopole directions, it mostly corrects the additional declination dispersion evident in the ChRM directions (if using only MTC component reorientation; see Fig. 8a) and captures the specimen declination dispersion within and between the core runs. With this procedure, three of the 49 studied runs could not be reoriented. The VGP_R from the jointly reoriented core runs for both the S-class and T-class ChRM sets are shown in Figure 7f. An estimate of the formational mean directions (Fig. 8c,d) are comparable to outcrop-based studies of these units.

The magnetostratigraphy for the core can be inferred from the specimen-level interpretations (both S-class and T-class data; Fig. 7d), the ChRM inclinations from the S-class data (Fig. 7e), and lastly, the VGP_R, which uses both the T-class and S-class data. The VGP_R lacks data for five sampling levels in three core runs, which could not be reoriented (Fig. 7f), but are shown with S-class specimen inclinations instead in Fig. 7e.

The resulting polarity displays four major magnetozone couplets (BM1n/BM1r to BM4n), with five of the magnetozones having submagnetozones (Fig. 7g). Submagnetozones BM1r.1n, BM3r.2n, BM3r.3n and BM3r.4r are defined by sampling from at least two adjacent depths, with one or more specimens from each depth. Tentative submagnetozones, BM1n.2r and BM3r.1n, with ¾ bar width, are defined by two specimens from a single sampling depth. Tentative submagnetozones, BM1n.1r, BM3n.1r, BM3n.2r and BM4n.1r, with a half or ¼ bar width, are defined by a single specimen at a single sampling depth.

Reverse polarity specimens defined by VGP_R are more strongly dependent on the T-class type demagnetisations than the normal polarity specimens (Fig. 7f). This issue is also apparent in the coeval section at StAB and in the overlying Hettangian (Hounslow *et al.*, 2004; Hüsing *et al.*, 2014), as well as in the youngest parts of the MMG in the Seaton sections (Hounslow & Gallois, 2023). As in the prior studies, this is attributed to the difficulty in fully removing the

https://doi.org/10.1017/S0016756825100162 Published online by Cambridge University Press

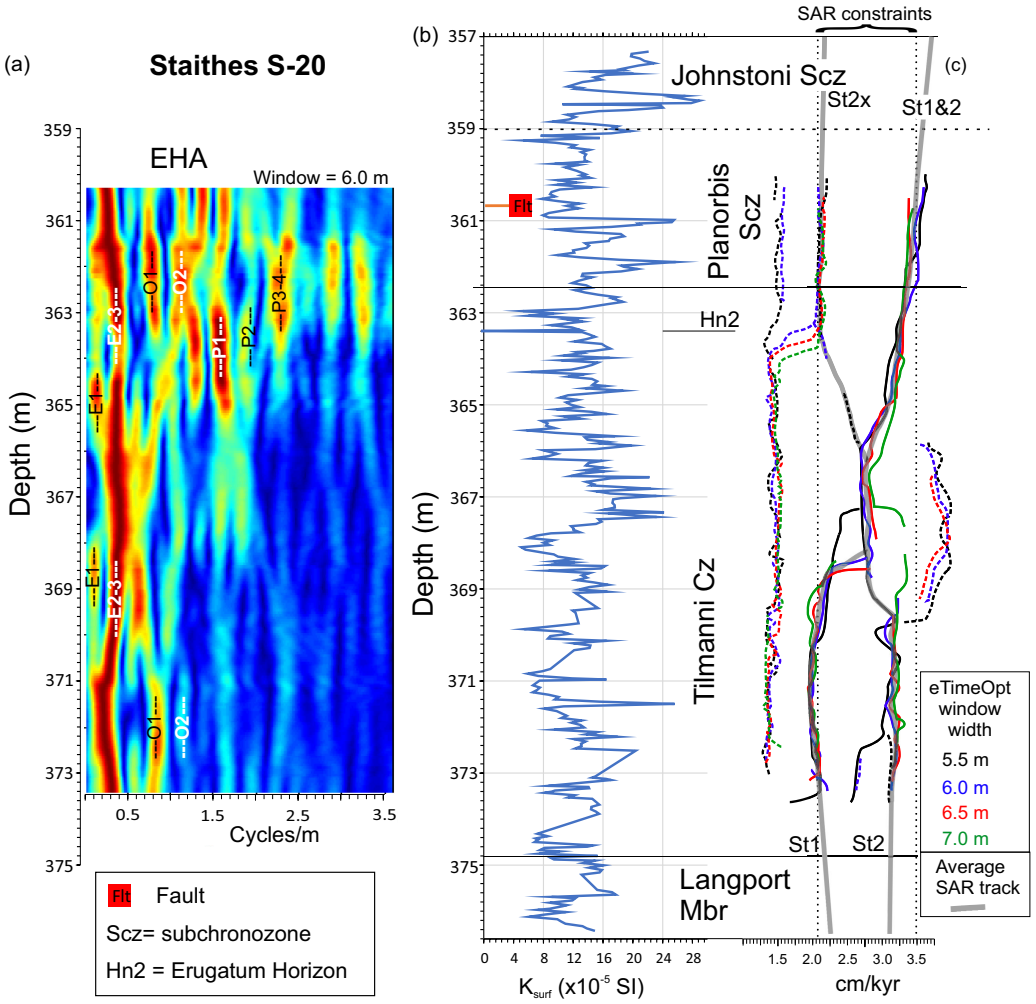

Figure 9. a) Evolutionary harmonic analysis (EHA) map for the Staithes S-20 K_{surf} data, with possible astronomical periods indicated (based on the SAR constraints). E=eccentricity cycles, O=obliquity, and P=precession (targets listed in SM Table S1); b) the S20 K_{surf} data with depth in metres; c) SAR tracks based on the evolutionary TimeOpt method (Meyers, 2019) for four width windows (5.5 m to 7.0 m; coloured lines); full lines are primary tracks and dashed lines secondary tracks. The SAR constraints (dotted vertical black lines) and inferred composite baseline SAR tracks (in thick grey line, St1, St2, St2x) are shown. Comparable plots for Lavernock, St Audrie's Bay and Lyme Regis are in SM Figs. S10 to S12.

much stronger Brunhes-age overprint magnetisation, which partially remains overlapped with the ChRM in the T-class specimens.

4.d. Astrochronology for the Langport Member and early Hettangian

4. d.1. SAR constraints

The dataset of Guex *et al.* (2012) from Peru provides an approximate duration for the Tilmanni plus Planorbis chronozones. An approximately linear SAR is suitable for their data, which extends from the latest Rhaetian to a level which can be correlated to the upper part of the Angulata Cz of the Hettangian (SM Fig. S9). However, correlation of the Peruvian ammonite assemblages to the European ammonite biochrons has some uncertainty, and two possible scenarios are used, which, in combination with the uncertainty in the radioisotopic dates, suggest that the duration of the Tilmanni plus Planorbis chronozones is between 0.725 and 1.175 Myr (SM Fig. S9). In combination with the thicknesses of these chronozones in the UK sections, the likely range in average SAR for sections at StAB, Lavernock, Lyme Regis and S-20 are 1.15–1.87 cm/kyr, 1.24–2.01 cm/kyr, 0.56–0.91 cm/kyr and 2.13–3.45 cm/kyr, respectively. These SAR constraints allow narrow windows of where to expect spectral peaks in cycles/m in the evolutive harmonic spectra. These are marked on Figure 9a for the S-20 dataset (and comparable plots in SM Figs. S10–S12 for the other sections). These simply demonstrate plausible astronomical periods in the data but have not been used beyond this illustration. To allow easier inter-section comparison of the predicted SAR from the durations derived by the astrochronology, the average SAR over the Tilmanni Cz and Planorbis Scz is normalised by the upper SAR constraint for each section, giving a variable $nSAR_{T+PS}$. This ranges from 1.0 at the longer duration constraint to 0.62 for the shorter duration constraint, irrespective of the section concerned.

4. d.2. Stage 1, evaluation of baseline SAR models

The evolutionary TimeOpt method (eTimeOpt) gives a variety of plausible SAR tracks which could yield an average SAR within the range of the SAR constraints. These tracks were based on the r^2_{opt} maps since these gave clearer tracks than the $r^2_{envelope}$ or $r^2_{spectral}$ eTimeOpt maps. The inferred possible SAR tracks for each section were based on visually estimating a mean path through the primary tracks (i.e., the stronger tracks). An example of this, using the S-20 dataset, is shown in Figure 9c, which generates two probable tracks (St1 and St2). An additional lower SAR track (St2x) was added from the secondary tracks since the Planorbis Scz is rather more condensed (or has more hiatuses) compared to the other sections and that in the Felixkirk borehole (Figs. 1a, 3a). The ratios of the thickness of the Planorbis Scz/Tilmanni CZ are 0.78, 0.73 and 0.73 at StAB, Lavernock and Lyme Regis, respectively, with the values at

https://doi.org/10.1017/S0016756825100162 Published online by Cambridge University Press

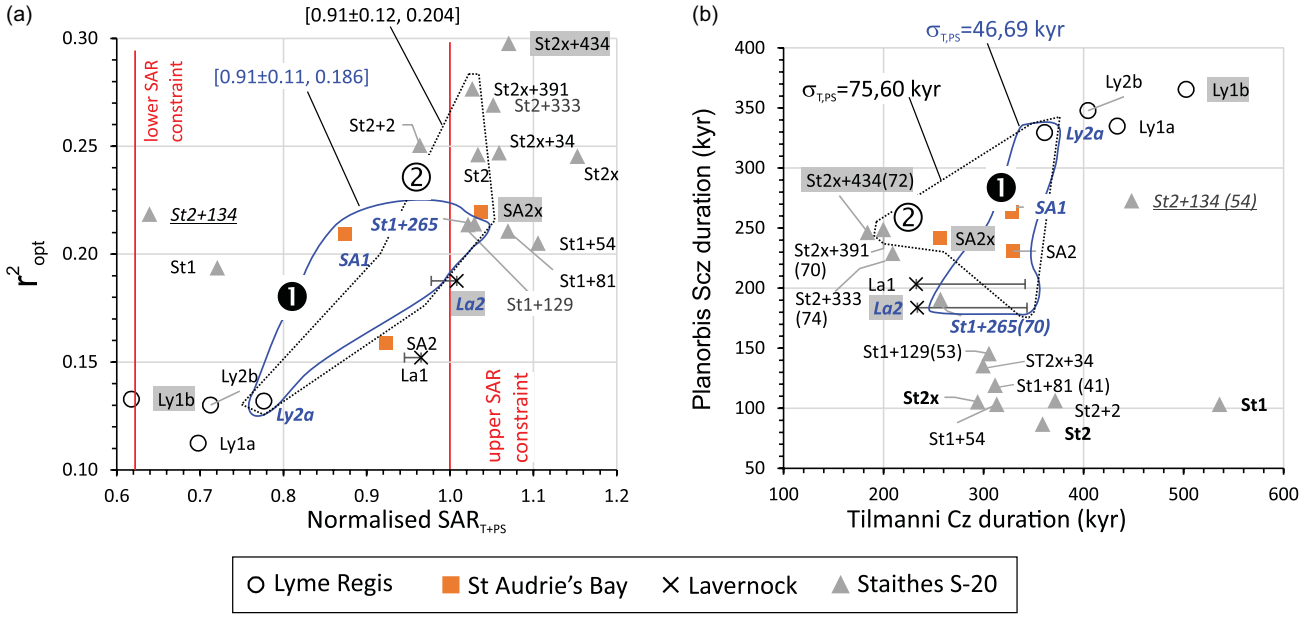

Figure 10. Evaluation of the baseline SAR models. SA= St Audrie's Bay (StAB), Ly=Lyme Regis, La=Lavernock and St= Staithes S-20 models, respectively. Those with an appended + indicate the hiatus (or missing interval) inserted (in kyr) into the baseline SAR model (only for S-20 models). a) shows the r^2_{opt} and the normalised SAR across the Tilmanni plus Planorbis chronozones interval ($nSAR_{T+PS}$), with the upper SAR constraint for each section being the normaliser (giving $nSAR_{T+PS}$ =1). b) Shows the durations of the Tilmanni Cz and Planorbis Scz. $\sigma_{T,P}$= standard deviation of the durations of the Tilmanni Cz and Planorbis Scz for the SAR sets indicated inside the marked regions (solid blue line for set-1). The numbers in a) inside [. . .] are the mean $nSAR_{T+PS}$ ±1σ and mean r^2_{opt} for the SAR sets inside the solid blue/black dotted lines (set 1 models marked in blue). The SAR model with the maximum r^2_{opt} in each section has a grey background. Examples of hiatus- testing data shown in SM Figs. S13 to 15.

Felixkirk and S-20 being 0.48 and 0.28. SAR tracks were similarly constructed for the other sections (SM Figs. S10c, S11c, S12c), yielding (stronger) primary-based tracks labelled as SA1 and SA2 at StAB, La1 and La2 at Lavernock, and Ly1a, Ly1b, Ly2a and Ly2b at Lyme Regis. At StAB, an additional larger SAR track (SA2x) was defined on secondary tracks, which also yields a mean SAR within the SAR constraints by joining the SA2 track in the mid part of the Planorbis Scz (SM Fig. S11c). This larger SAR may account for the expansion of Hn5 in the lower part of the Planorbis Scz (Fig. 3b). The primary SAR tracks for Lavernock suggest a possible lower SAR in the upper part of the Tilmanni Cz in a mudstone-rich interval (between the 'Dual Bed' and bed 30; Waters & Lawrence, 1987) as in SM Figure S10c with larger K_{surf} (Fig. 3c).

Using TimeOpt, the largest r^2_{opt} were for the baseline SAR models St2, SA2x, La2 and Ly1b (Fig. 10a). At Lavernock, the proxy base of the Tilmanni Cz (at the base of the Watchet Beds) was projected downwards using the average SAR in the overlying part of the chronozone (extension bars on La1 and La2 models in Fig. 10). In S-20, the best-performing St2 model (r^2_{opt} =0.246) does not correct for the shorter Planorbis Scz (Fig. 3a), with all the S-20 baseline models (St1, St2, St2x) yielding briefer Planorbis Scz durations compared to the other sections (Fig. 10b).

A comparison of the K_{surf} correlations to S-20 suggests there may be a missing part around the Hn6 to Hn8 interval (Fig. 3a). If the ratio of the thicknesses of the Planorbis Scz/Tilmanni Cz at Felixkirk is applied to S-20, it suggests that ~2.5 m may be missing at S-20, representing ~42% of the Planorbis Scz. This is inferred to be related to a level in the core with near-horizontal slickensides at 1183.38 ft (360.68 m), which probably represents a small fault, providing a position for the missing interval and 'hiatus'. Therefore, for this initial evaluation, the missing interval was estimated using hiatus testing applied to the S-20 SAR baseline models (see SM Figs. S13 to S15 for hiatus testing examples). These yielded nine additional models with larger r^2_{opt} (Fig. 10a) for the baseline models St1, St2 and St2x, with only St2+134 having a lower r^2_{opt} (by 0.028) than the St2 baseline model (the '+ number' is the hiatus in kyr inserted into baseline models prior to TimeOpt optimisation; SM Fig. S15). It is important to recognise that these initial baseline hiatus durations will not correspond to the hiatus durations inferred after optimisation using TimeOpt (note the longer 'hiatuses' than Planorbis Scz durations (on the y-axis) for models St2+333 and St2x+434; Fig. 10b). The percentage of the Planorbis Scz duration represented by the 'hiatus' in the optimised age model is shown in brackets after the 'model code+hiatus' in Figure 10b (only for those with values >40%). Many of these hiatus models still yield briefer Planorbis Scz durations but similar Tilmanni Cz durations, compared to other section baseline models. The exceptions are St2x+434, St2x+391, St2+333 and St1+265 (Fig. 10b), which yield Planorbis Scz durations like the other sections. These also yield $nSAR_{T+PS} > 1.0$, apart from St2+2 and St2+134 (Fig. 10a).

Selecting those with the larger r^2_{opt} and minimal dispersal in zonal durations and $nSAR_{T+PS}$, a plausible solution using all four section datasets is using SAR models SA1, La2, Ly2a and St1+265 (those inside the area marked with a blue solid line in Fig. 10a, b). This set has duration dispersion for the Tilmanni Cz and Planorbis Scz ($\sigma_{T,PS}$) of 46 and 69 kyr, respectively, (top of Fig. 10b), and has a σ for $nSAR_{T+PS}$ of 0.11 (top of Fig. 10a). This set (Set-1) of SAR models contains one with the largest section-based r^2_{opt} (i.e., La2) and a combined mean r^2_{opt} of 0.186 (top of Fig. 10a). Ideally, a good solution should maximise the overall r^2_{opt} (i.e., the astronomical target fits), contain more of the solutions with the largest section-based r^2_{opt} and provide greater intersection consistency in $nSAR_{T+PS}$ and biochron durations. A second group of SAR models with a larger mean r^2_{opt} of 0.204 are La2, Ly2a, SA2x and St2x+391 (Set-2), which give $\sigma_{T,PS}$ = 75, 60 kyr, and σ for $nSAR_{T+PS}$ of 0.12

https://doi.org/10.1017/S0016756825100162 Published online by Cambridge University Press

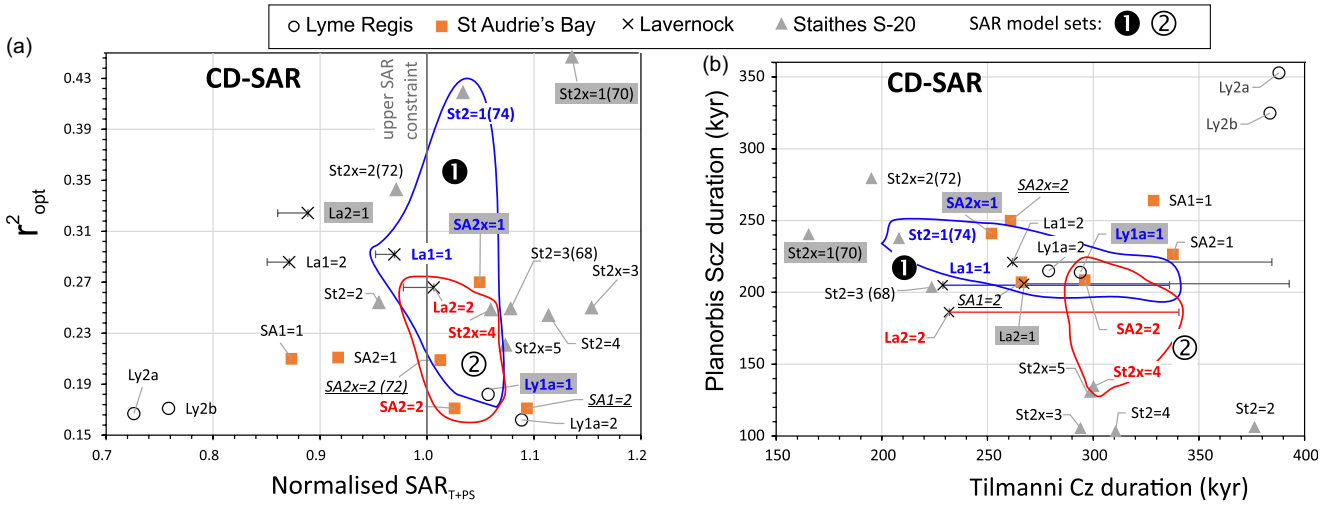

Figure 11. β- testing of the better-performing baseline models from Figure 10 without hiatus (except for the Staithes S-20 dataset), for the CD-SAR type models. Plot of r^2_{opt} with respect to β shown in Fig. 12a. Labelling details as in Figure 10. SAR model set 1 and 2 statistics in Table 1. The equivalent TS-SAR models are shown in SM Figure S16.

(inside the area marked with dashed black lines in Fig. 10a, b). This highlights that there may not be a single outstanding solution but one or more similar alternatives. Many of the S-20 SAR models with larger r^2_{opt} suggest the hiatus may occupy about 70% of the Planorbis Scz (models St2x+434, St2x+391, St2+333, St1+265; Fig. 10b), which is larger than the ~42% expected (compared to Felixkirk). Such large percentages could also relate to the uncertainty on the *Caloceras* species, which may be Johnstoni Scz, Hn11–11b, rather than Hn10, pointing to a greater loss of the upper part of the Planorbis Scz (alternative on Fig. 3a).

4. d.3. Stage 2, modulation of the baseline SAR models

The better-performing models from stage-1 were used for β-testing, searching for maximum r^2_{opt} with respect to β-values selecting peaks in r^2_{opt} values greater than or similar to the stage 1 models. High values of mod(β) (when $SAR_{β,H}$ approached the limit possible) generally yield unrealistic age models, since the levels with very low $SAR_{β,H}$ introduce many hiatus-like intervals into the SAR section models, giving a region of r^2_{opt} instability at large |β|. Therefore, for the β-H search region, a lower |β| outside this regional of instability was used (see examples in SM Figs. S28–S30). In addition, for the S-20 models containing the faulted-missing interval, this was treated to β-H testing as described in Sections 3.c.1 and 4.d.4.

The resulting models are labelled with the baseline SAR model plus '=n', where n is the rank of the r^2_{opt} value, with '=1' indicating the largest r^2_{opt} value ('=2' next largest, etc, and '=0' if only one r^2_{opt} peak) for that baseline SAR model (CD-SAR type models in Fig. 11; TS-SAR type models in SM Fig. S16). Most of these models have larger r^2_{opt} (Fig. 11a) than baseline models from stage-1, a model-specific change symbolised as Δr^2_{opt}. Of these, the median Δr^2_{opt} for the CD-SAR models are 0.050 and 0.031 for the TS-SAR type models, with the maximum Δr^2_{opt} of 0.201 for the S-20 CD-SAR model St2x=1 (Fig. 11a). On a section-specific basis the maximum Δr^2_{opt} are shown by the CD-SAR models for S-20 (of 0.201; St2x=1) and Lavernock (of 0.140, La1 = 1; Figs. 11a, 12a) and by the TS-SAR models for StAB (of 0.067, SA2=1) and Lyme Regis (of 0.179, Ly1a = 0, SM Fig. S17). Hence, based on TimeOpt, the CD-SAR type models seem slightly better overall, but not universally for all sections.

For the CD-SAR type models (with negative β; Figs. 11, 12a), there are two sets of models (Set-1 and Set-2) which have low dispersions in $nSAR_{T+PS}$ and biochron durations (Table 1; Fig. 11). These share the Ly1a = 1 model but have differing models for the S-20, Lavernock and StAB models. Set 1 maximises mean r^2_{opt} and Δr^2_{opt} (of 0.291, 0.121; Table 1), with minimum dispersion in Planorbis Scz durations. Set 2 has lower dispersion in Tilmanni Cz durations (Table 1). Both sets show larger mean r^2_{opt} than the sets for the baseline models (Table 1). The models in these sets have a wide range of β values (Table 1; Fig. 12a). The power spectra show more prominent matches to the eccentricity and obliquity bands, although model SA2x = 1 is a fair match in the precession bands (Fig. 12b).

For the TS-SAR type models, the section-specific models with the largest r^2_{opt} are somewhat scattered in the chronozone duration graph (SM Fig. S16d), and the best choice is a single set with minimum dispersion in $nSAR_{T+PS}$ and chronozone duration (Table 1; SM Fig. S16b,d); this includes the SAR model at Lyme Regis with the largest r^2_{opt}. Apart from the Ly1a=0 model, others in this set have low +β values (Table 1; SM Fig. S16a).

From the β-testing, the CD-SAR models seem to have better overall performance for the following reasons.

1) More of the SAR models from each section have the larger r^2_{opt} and cluster in the zonal duration plots better, rather than being more dispersed as in the TS-SAR models (Table 1).

2) The set-1 in the CD-SAR models includes two of the models with the largest r^2_{opt} for each section, rather than one in other sets (Fig. S11a; SM Fig. S16b). This set also has the largest mean Δr^2_{opt} of 0.121 (Table 1).

3) There is a general positive relationship between Δr^2_{opt} and increased SAR modulation amplitude measured by mod(β) for the CD-SAR models when all the section datasets are considered together (SM Fig. S17a).

4) The mostly low β- values for the models comprising the one set for the TS-SAR models indicate that, except generally for the Lyme Regis models, the SAR modulations expressed by +β have limited impact on improving the astronomical fits (SM Fig. S17b).

https://doi.org/10.1017/S0016756825100162 Published online by Cambridge University Press

Table 1. Data for the sets of baseline and combined β-testing duration models are indicated in Figs. 10, 11, 12 and SM Figure S16. In column 1, H_{opt} is the hiatus inferred by the TimeOpt optimised age models shown inside round brackets, as well as the that inserted in the baseline age model (shown as H), with both in kyrs. Column 6: the statistical significance values (P(AR1')) of the model using a Monte Carlo simulation of an AR1 process (Meyers, 2019), with values listed in the same model order as in column 1 (1000 simulations with 100 sedimentation rates). The AR1 process is modelled with 'raw' ρ values for S-20, StAB, Lavernock and Lyme of 0.7325, 0.6189, 0.7481 and 0.7639, respectively. Δ r^2_{opt} = the mean improvement in r^2_{opt} over the baseline models in Figure 10

1. Model/Set: SAR model [β, H] (H_{opt})	2. Tilmanni Cz. duration (kyr)	3. Planorbis Scz. duration (kyr)	4. $nSAR_{T+PS}$	5. Mean r^2_{opt}	6. P(AR1')	7. Δ r^2_{opt}
Baseline SAR models (Fig. 10a,b)						
1: St1+265(133), SA1, La2, Ly2a	323 ± 46	242 ± 69	0.91 ± 0.11	0.186	0.88,0.01,0.76,0.81	–
2: St2x+391(173), SA2x, La2, Ly2a	290 ± 75	251 ± 60	0.91 ± 0.12	0.204	0.57,0.01,0.76,0.81	–
***β*-testing: CD-SAR models** (Figs. 11, 12)						
1: St2=1 [-0.8,360] (176), SA2x=1 [-0.20,0], La1=1[-0.19,0], Ly1a=1 [-0.268,0]	273 ± 55	224 ± 18	1.03 ± 0.04	0.291	0.074,0.01,0.13,0.53	0.121
2: St2x=4 [-0.01,32] (21), SA2=2 [-0.062, 0], La2=2 [-0.168,0], Ly1a=1 [-0.268,0]	308 ± 22	186 ± 36	1.04 ± 0.03	0.217	0.72,0.057,0.24,0.53	0.059
***β*-testing: TS-SAR models** (SM Fig. S16)						
1: St2=3 [0,333] (170), SA2x=0 [0.036, 0], La2=3 [0.104, 0], Ly1a=0 [0.375, 0]	275 ± 81	241 ± 35	1.00 ± 0.07	0.241	0.82,0.01,0.71,0.11	0.063

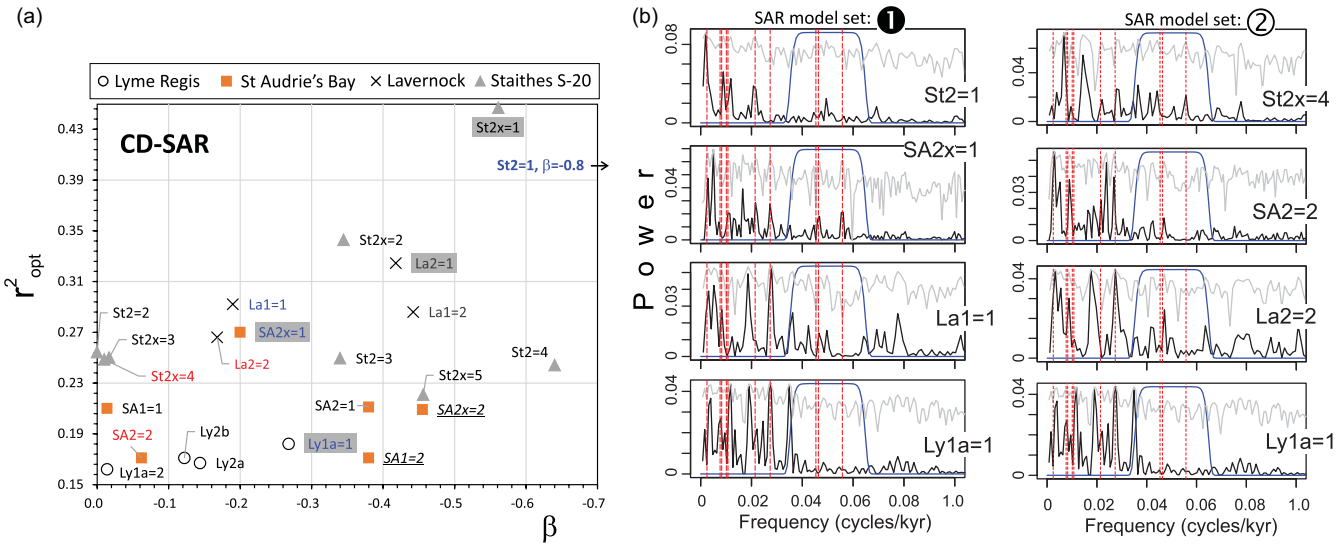

Figure 12. a) Plot of r^2_{opt} with respect to β for the CD-SAR β-testing models in Fig. 11. Labelling details as in Figure 10. b) Power spectra of the SAR models included in SAR model sets 1 and 2 from Fig. 11, with linear (black) and logarithmic scaling of spectra (in grey), and eccentricity, obliquity and precession frequencies (red vertical dashed-lines) as in SM Table S1. Blue line is the bandpass filter for evaluation of the precession amplitude envelope.

5) Although none of the CD-SAR sets fully regularise with time the correlation of the ammonite biohorizons, they generally perform better in this respect than the best TS-SAR model set (SM Figs. S21 to S23).

6) Monte Carlo tests of the models against an AR1 process indicate overall that CD-SAR models in set-1 have a closer approach or exceed the 95% confidence level (P(AR1') <0.05) in more cases (Table 1). For the TS-SAR models only, Ly1a=0 has lower P(AR1') compared to the corresponding Lyme Regis model for CD-SAR set-1 (Table 1).

However, most of the Lyme Regis TS-SAR models give larger Δr^2_{opt} values than those using the CD-SAR type models at this site (SM Fig. 17b), accounting for the smaller P(AR1'). The opposite is the case for the Lavernock models, which show much improved Δr^2_{opt} for the CD-SAR type models (SM Fig. 17a). If the β-values usefully express the degree of SAR modulation at the bedding scale, the expectation would be that StAB and S-20 should behave similarly (i.e., similar scale of β) since these contain fewer limestones than the Lavernock and Lyme Regis sections, datasets which also might be expected to have similar behaviour. However, this simple concept could be flawed, and the difference between the responses in the Lyme Regis and Lavernock datasets to β-testing might reflect more fundamental differences in the bedding-scale SAR modulation between those sections. This difference in behaviour might reflect relative contributions and timing of diagenetic carbonate formation or the differing land-proximal to distal shelf positions of these sections. This could yield a differing style of SAR modulations, which could be compatible with evidence for condensation/tractional erosion in some limestone beds at Lyme Regis (Weedon *et al.*, 2018; Paul *et al.*, 2008). The inclusion of the Ly1a baseline model (Ly1a is ranked top in each case) in the sets for both the CD-SAR and TS-SAR models suggests

https://doi.org/10.1017/S0016756825100162 Published online by Cambridge University Press

Table 2. Data for the sets of combined β-H duration models indicated in Figures 13, 14 and SM Figs. S18, S19. In column 6, H_{opt}= the hiatus inferred by the TimeOpt optimised age models (in the same model order as in column 1), rather than that inserted in the baseline age model (shown as H, kyrs in column 1). Other columns as in Table 1

1. Model/Set: SAR model [β, H(kyrs)]	2. Tilmanni Cz. duration (kyr)	3. Planorbis Scz. duration (kyr)	4. $nSAR_{T+PS}$	5. Mean r^2_{opt}	6. H_{opt} (kyrs)	7. P(AR1')
β-H testing: CD-SAR models (Figs. 13, 14)						
1: St2=1 [-0.80,360], SA2x=1 [-0.156,1], La1=1 [-0.19,0], Ly1a=1 [-0.0015,119]	265 ± 53	239 ± 28	1.01 ± 0.04	0.321	176, 0.9,0,73	0.074,0.01,0.13,0.065
2: St2x=4 [-0.01,32], SA2x=3 [-0.346, 96], La2=2 [-0.168,0], Ly1a=3 [-0.049,15.6]	299 ± 30	184 ± 36	1.06 ± 0.04	0.240	21,71,0,10	0.74,0.01,0.24,0.31
3: St2=5 [-0.228,257], SA2=3 [-0.012,81], La1=2 [-0.442,0], Ly1a=2 [-0.261,57]	397 ± 32	258 ± 44	0.79 ± 0.11	0.223	150,60,0,35	0.79,0.058,0.195,0.29
β-H testing: TS-SAR models (SM Fig. S18)						
1: St2=3 [0.000,333], SA2x=1 [0, 1.5], La2=3 [0.104, 0], Ly1a=1 [0.33, 39.8]	278 ± 80	236 ± 27	1.00 ± 0.08	0.251	170,1.4,0,20	0.82,0.01,0.71,0.038
β-H testing: CD-SAR models: SA, St, La, TS-SAR models: Ly (SM Fig. S19)						
Final: St2=1 [-0.80,360], SA2x=1 [-0.156,1], La1=1 [-0.19,0], Ly1a=1 [0.33,39.8]	262 ± 53	238 ± 27	1.02 ± 0.04	0.325	176,0.9,0,20	0.074,0.01,0.13,0.038

that this SAR model is the best irrespective of the type of applied modulation (i.e., Ly1a = 1, Ly1a = 0; Table 1).

4. d.4. Stage 3, Hiatus and β–testing of the baseline SAR models

Detection of hiatuses in the Lias Gp has been based on identifying missing biostratigraphic intervals, sedimentological evidence of hiatus, or steps in Shaw plots based on correlation of biohorizons (Weedon *et al.*, 2018, 2019). Whilst these approaches have merit, two of them are built on assumptions of strictly isochronous biohorizons, uniformity of ammonite preservation and near-linear SAR expectations embedded into their use. Ideally, cases of combined sedimentological and biostratigraphic evidence of hiatus provide the stronger conclusive cases, but these are lacking in the interval examined here. Perhaps the best evidence for hiatus is the absence or thinness of Hn3 (Fig. 3) at the base of the Planorbis Scz (Weedon *et al.*, 2018). Biohorizons Hn6 and Hn5 are also relatively condensed at Lyme Regis and Lavernock, a feature used by Weedon *et al.* (2019) to infer hiatuses. Although this feature may correspond approximately with a maximum flooding surface in the central European Basin, which is provisionally dated at about Hn7 to Hn8 (Barth *et al.*, 2018). In the present work, a more conservative view is used, in that hiatuses may exist at the base of the Planorbis Scz at StAB and Lyme Regis (Fig. 3b, d). In addition, it is also impractical to insert two hiatuses and vary β simultaneously.

The better-performing baseline SAR models were tested simultaneously for variation in hiatus (H) and β. The hiatus search window ranged from 0 kyr to upper values identified from hiatus testing, which gave realistic models (i.e., shown in SM Fig. S20). Inserting hiatuses at the base of the Planorbis Scz (for StAB and Lyme Regis datasets) using the better-performing SAR models tends to give comparable or slightly lower dispersion in estimates of $nSAR_{T+PS}$ and biochron durations to those from β-testing alone (Tables 1, 2).

The resulting CD-SAR models give three possible groups: set-1 to 3 (Fig. 13). Set-3, marked with a dotted red line in Figure 13, gives low and dispersed $nSAR_{T+PS}$, the largest Tilmanni Cz duration (Table 2), and the smallest mean r^2_{opt} and is not considered further. The set-1 and set-2 statistics for these CD-SAR models are rather like the comparable models from β-testing, since they include the same models or models with similar β and H (Tables 1, 2). This is except for the included Lyme Regis models. Although set-1 has the largest mean r^2_{opt} of 0.321 of the CD-SAR models, the 73 kyr hiatus using the Ly1a = 1 model is unrealistically large at 31% of the Planorbis Scz duration (SM Fig. S21). Accepting the hypothesis that the TS-SAR type models may be more appropriate for the Lyme Regis dataset would give an alternative final set of models, which include the CD-SAR models at the other locations (bottom panel set-final in Table 2 and grouping plots in SM Fig. S19). These give a marginally larger mean r^2_{opt}, a smaller hiatus and a lower P(AR1') for the included Lyme Regis model (Table 2). Hence, our final optimum estimates for the durations of the Tilmanni Cz and Planorbis Scz give 262 ± 53 kyrs and 238 ± 27 kyr, respectively (means: r^2_{opt} = 0.325 and $nSAR_{T+PS}$ = 1.02±0.04; Table 2). Whilst some refinement could be achieved on the Tilmanni Cz duration if the TJB position were more precisely known in each section, the 1σ uncertainty of ±53 kyrs is comparable to the uncertainty on the TJB position at StAB (compare Fig. 3b, SM Fig. S22).

This optimum estimate is just above the upper limit of the expected SAR based on data in Section 4.d.1. For comparison at StAB, using the duration of the Tilmanni Chronozone+ Planorbis Scz would give $nSAR_{T+PS}$ of 0.49, 2.20 and 1.86 using the timescales in Weedon *et al.* (2019), Husing *et al.* (2014) and Ruhl *et al.* (2010), respectively. At Lavernock and Lyme Regis, the equivalent $nSAR_{T+PS}$ would be 0.42 and 0.52, respectively, using the estimates of Weedon *et al.* (2019). Our final duration estimates therefore fall between those of the earlier studies and are ~50% of those suggested by Weedon *et al.* (2019) and longer by x2.2 and x1.8 than those suggested by Hüsing *et al.* (2014) and Ruhl *et al.* (2010).

4. d.5. An anchored astrochronology for the early Hettangian

To anchor this astrochronology, the radioisotopic dates from the Levanto section in Peru are correlated to the StAB section using the correlation relationships between the organic carbon isotope records proposed by Ruhl *et al.* (2020, fig. 3). This places the base of

https://doi.org/10.1017/S0016756825100162 Published online by Cambridge University Press

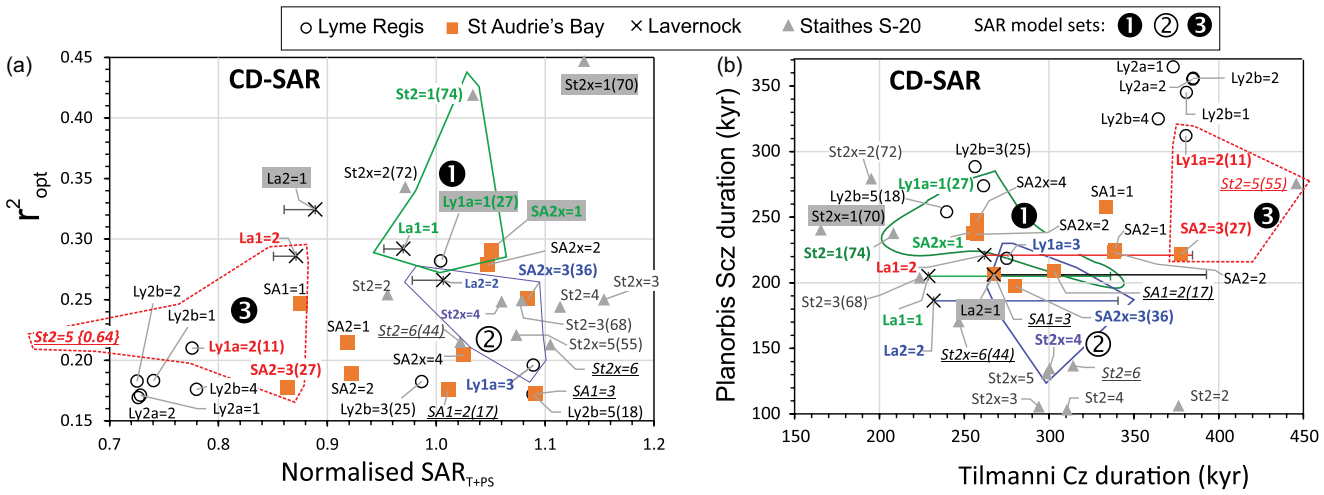

Figure 13. β-H- testing of the better-performing baseline models from Figure 10 with hiatus inserted at the base of the Planorbis Scz for Lyme Regis and StAB models. Plot of r^2_{opt} with respect to β shown in Fig. 14a. Notation details as in Figures 10 and 11. SAR model set-1, set-2 and set-3 statistics in Table 2.

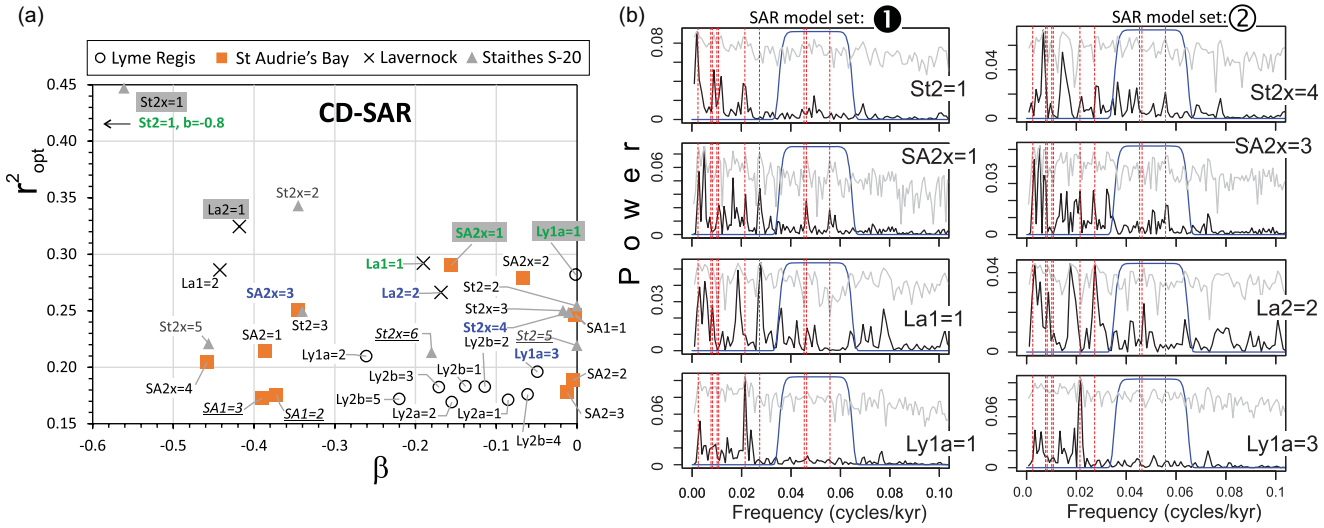

Figure 14. a) Plot of r^2_{opt} with respect to β for the CD-SAR β-H- testing models in Fig. 13. Labelling details as in Figure 10. b) Power spectra of the SAR models included in sets-1 and set-2 from Fig. 13, with linear (black) and logarithmic scaling of spectra (in grey), and eccentricity, obliquity and precession frequencies (red vertical dash-lines) as in SM Table S1. Blue line is the bandpass filter for evaluation of the precession amplitude envelope.

the Tilmanni Cz close to the base of magnetozone SA5r (Figs. 3b, 15). These relationships were enhanced by utilising an estimate of the stratigraphic uncertainty in this correlation in the stratigraphic metre scale at StAB. The projected positions and uncertainties were estimated by projecting the Peruvian dates onto the duration scale for the SA2x =1 CD-SAR model (model in set-final), which was projected downwards into the CMbr and the WFm (Fig. 15). The age of the base of the Lias Group is estimated by fitting a regression line between the duration scale and the radiometric dates using uncertainty in both axes (York's method; Read, 1989; Excel script by P. Kromer) shown as a solid blue line in Figure 15. The three dates spanning 201 to 201.6 Ma were used since these are reasonably well-constrained correlations, and the dates fall on a linear trend. This gives a basal Lias Gp age of 201.394 Ma, which was used to anchor the astrochronology. If there was a perfect match between the astrochronological durations and the correlated radioisotopic dates, lines parallel to the black fixed-duration line in Figure 15 would be expected. Clearly this is not case for all these dates, either because the SAR changes in parts of the section, the correlations of the radioisotopic dates are incorrect, or the dates themselves are biased. Date LM4 117/118 is clearly inconsistent for one or more of these reasons. The regression fit has a lower gradient than the fixed-duration line, possibly because of a lower SAR in the upper part of the StAB section shown. Date LM4 76/77 may also be part of the regression trend if projected downwards. An alternative possibility is that dates LM4 76/77 and LM4 58/59 may reflect an SAR close to the fixed-duration line when projected down from the top of the WFm (dotted line in Fig. 15). If this were the case, there would be a c. 100 kyr hiatus at around the base of the CMbr. Significantly, the coeval nature of magnetozones E23r and

https://doi.org/10.1017/S0016756825100162 Published online by Cambridge University Press

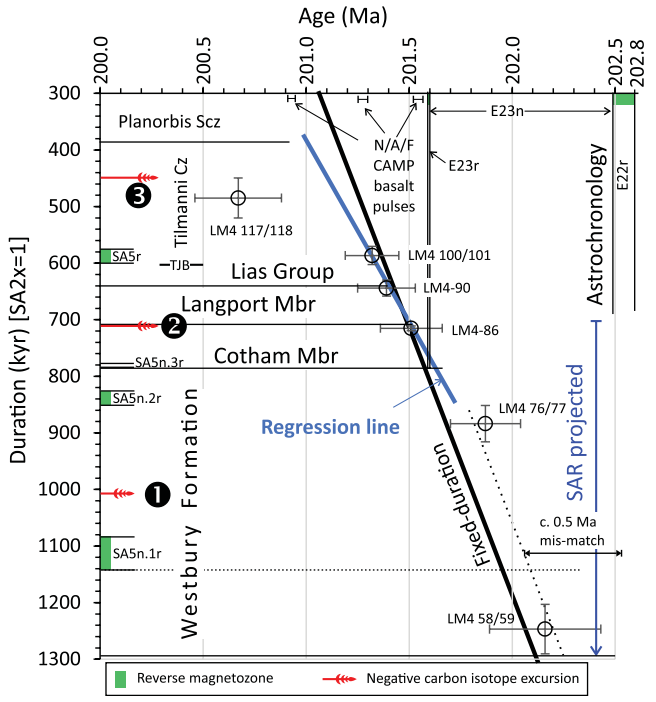

Figure 15. Radioisotopic dates from Peruvian sections (Guex *et al.*, 2012; Wotzlaw *et al.*, 2014) correlated with the St Audrie's Bay (StAB) section using organic carbon isotope excursions as in Ruhl *et al.* (2020). Each of the dates (circles) has horizontal and vertical error bars representing the 2σ age uncertainty, and the estimated stratigraphic uncertainty (in the duration scale of the SA2x=1 age model), respectively. Reverse magnetozones and negative carbon isotope excursions at StAB as in Figure 16. Ages of Newark Basin (N), Argana Basin (A) and Fundy Basin (F) CAMP pulses from Blackburn *et al.* (2013). The x-axis age scale shows Newark 'E' magnetozones from Kent *et al.* (2017). The blue regression line is a fit to the dates LM4-86, LM4-90 and LM4 100/101, using the method of Reed (1989). Black fixed-duration line is a fit to the same three dates, using a weighted regression fit, but with a fixed slope to match the durations in both x and y scales. TJB= Triassic–Jurassic boundary age from Wotzlaw *et al.* (2014) projected onto the SA2x=1 age model.

SA5n.3r is demonstrated with these correlations and chronometric estimates, with magnetozone bases falling between the regression-fit and the fixed-duration fit at ~201.60 Ma.

Using the regression fit (and CD-SAR model SA2x =1 for scaling) gives ages of 201.609 Ma and 201.494 Ma for the bases of the CMbr and Langport Mbr respectively at StAB. Following the same procedure, ages for the Marshi, Spelae and top Tilmanni CIE's at StAB are 201.936 Ma, 201.499 Ma and 201.113 Ma, respectively. The uncertainty of these ages is on a similar scale to those on the chronozone durations, with a minimum of c. 50 kyr (not including uncertainty from radioisotopic dates).

5. Discussion

5.a. The Norian–Rhaetian boundary interval

The following relationships for the S-20 dataset can be inferred by comparison with the same successions previously studied at StAB, Seaton, and Lavernock (Fig. 16).

In S-20, the Blue Anchor Fm is of normal polarity, but in the StAB, Seaton and Lavernock sections it is dominantly of reverse polarity (left columns in Fig. 16). Only the Williton Mbr at StAB is of normal polarity. This indicates that the Blue Anchor Fm in S-20 is not coeval with the Rydon Mbr in that formation in SW England. The most likely possibility is that the Blue Anchor Fm in S-20 is only coeval with the Williton Mbr of the Bristol Channel Basin. Therefore, the bulk of the Rhaetian-1 interval (magnetochrons UT22r–UT24r) can be inferred to be missing from the S-20 core (Fig. 16).

In S-20, the BM1n– BM3n polarity interval in the Branscombe Mudstone Fm is a reasonable match with those from StAB (SA2n–SA3n), Lavernock (LP2n–LP3n), and the Newark Supergroup (E15n to E17n) in the eastern USA (Fig. 16). The same interval is present in the Upper Chinle Fm farther west in the USA and in the marine biochronology-based geomagnetic polarity timescale (GPTS-B; Fig. 16). Correlations of Sevatian age sections between SW England and those in North America have been suggested by Hounslow *et al.* (2004), Kent *et al.* (2017), Hounslow & Gallois (2023) and Hounslow & Andrews (2024). Within BM1r, the submagnetozone BM1r.1n is probably coeval with E15r.1n in the Newark Supergroup, CC6r.1n in the Upper Chinle Formation and UT21r.1n in GPTS-B (Fig. 16).

Correlatives of the reverse submagnetozones in BM1n in S-20 have also been detected in the coeval CC6n in the Chinle Formation, PM10n at Pizzo Mondello (Kent *et al.*, 2017) and the F+ magnetozone at Kavur Tepe (see Hounslow & Muttoni, 2010 for details). These reverse submagnetozones are expressed within UT21n in the biochronology-constrained GPTS-B, within the earliest Sevatian (Fig. 16).

In S-20, the UT22r–UT24r hiatus is placed at the top of the variegated interval, probably at the anhydrite-rich bed at 394.91 m (1304.2 ft), with the overlying 0.3 m showing transitional character into the basal Blue Anchor Fm (SM Figs, S1f, S3d). The uppermost sample in the Branscombe Mudstone Fm is of reverse polarity and is tentatively considered equivalent to part of magnetozone SA4r/UT24r (Fig. 16). The Norian–Rhaetian boundary interval (NRB1 to NRB2) is placed within this substantial hiatus, which is associated (Fig. 1b) with the combined D5.1 and D5.2 disconformities in the Germanic Keuper (Barnasch, 2010).

5.b. Rhaetian 2 to 4 and the Penarth Group

The magnetic polarity timescale through the Rhaetian-2 to Rhaetian-4 is currently not entirely resolved, although this interval is largely dominated by normal polarity (Fig. 17). Broadly, there are two options for Rhaetian-3. The first is shown as GPTS-B in Figure 16, with two major reverse magnetochrons, UT25r and UT26r, in Rhaetian-2 and Rhaetian-3, respectively. This option largely derives from the conodont-dated Oyuklu section in Turkey (Gallet et al., 2007), a more poorly dated Argana Basin (Morocco) section (Deenen *et al.*, 2011), and the Newark Basin, eastern USA, datasets (Kent *et al.*, 1995; Kent *et al.*, 2017). The base of the Oyuklu section is probably truncated by two thrusts, which may have removed a substantial part of Rhaetian-1 (below the shown part in Fig. 17). The reference pattern for UT25r–UT26r is based on the Newark Basin succession, which is well constrained near the TJB (see Hounslow & Gallois, 2023).

The alternative option for the UT25r – UT26r interval is mostly derived from sections in the Lombardian Basin (northern Italy) and is shown next to the GPTS-B (Fig. 17). The Lombardian sections have limited biostratigraphic age control, other than in the latest Rhaetian-4 and from conodonts in the ZU1 interval of the Zu Limestone Fm, below the parts of the section with a magneto-stratigraphy; but they do have a detailed $\delta^{13}C_{org}$ record (Fig. 17). These sections display considerably more reverse polarity in UT26.

Reconciling these options requires either that substantial parts are duplicated and/or missing from ZU3a–ZU3b in the Brumano

https://doi.org/10.1017/S0016756825100162 Published online by Cambridge University Press

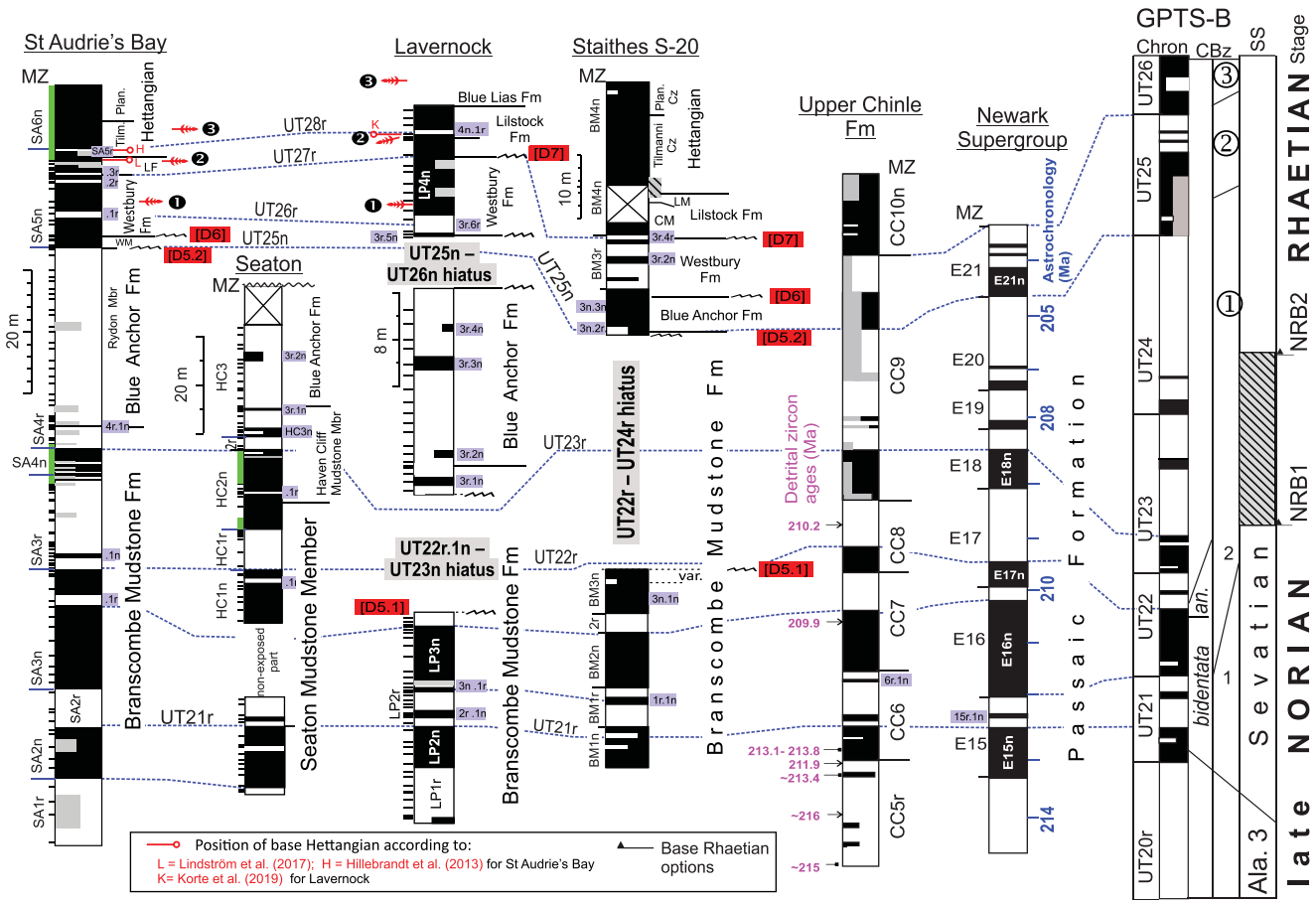

Figure 16. Comparison of the Staithes S-20 core magnetostratigraphy with other equivalent sections through the Sevatian and early Rhaetian. Other section data: St Audrie's Bay (StAB) (Hounslow *et al.*, 2004; Hüsing *et al.*, 2014), Seaton, Upper Chinle Fm composite and GPTS-B from Hounslow & Gallois (2022), Lavernock (Hounslow & Andrews, 2024), Newark Supergroup (Kent *et al.*, 2017). Sampling levels marked as ticks on the Seaton, StAB and Lavernock columns, shown as a green bar when densely sampled. Astrochronologic age (in blue) anchored to the Orange Mountain Basalt (Kent *et al.*, 2017). Hatching in the S-20 column represents uncertainty regarding the position of the base Hettangian in the core. CBz= conodont biozone, SS=Substage, Ala.3= Alaunian 3. Magnetozone (MZ) names from data sources. Additional abbreviations in key to Fig. 17.

section in Lombardy or that parts are missing from UT26n in both the Newark Basin and Oyuklu sections. A fault in E22n in the Martinsville core in the Newark Basin (Kent *et al.*, 1995; Olsen *et al.*, 1996) could account for part of this missing interval (Fig. 17). Some 0.7 Myr missing would bring the predicted Rhaetian durations derived by Galbrun *et al.* (2020) and Kent *et al.* (2017) closer together.

Mercury contents from multiple locations associate CAMP volcanism with the end-Triassic extinction and the Spelae CIE, which is in the upper part of the CMbr to basal Langport Mbr (Yager *et al.*, 2021). This relationship is confirmed by the correlated radioisotopic dates (Fig. 15). These all suggest that E23r in the Newark Basin and coeval submagnetozones in the Argana and Fundy basins (Deenan *et al.*, 2011), immediately prior to the onset of CAMP, are equivalent to SA5n.3r at StAB (Fig. 15), BM3r.4r in the basal CMbr in S-20, and UT27r in the GPTS-B (Fig. 17). A single-sample reverse magnetozone is also present in the uppermost part of the Zu Limestone Fm in the Lombardian Basin, which may represent the equivalent of UT27r ≡E23r (≡ symbolises coeval magnetozones or magnetochrons).

There is a dominance of reverse polarity in the WFm in S-20, but conversely of normal polarity in the WFm at StAB and Lavernock (Fig. 16). The simplest explanation is that differing amounts are missing because of hiatuses at the base and top of the WFm, which are inferred to be the D6 and D7 disconformities of the Germanic Keuper (Figs. 1b, 16). Possible explanations are that magnetozone BM3r at S-20 is equivalent to UT25r or that BM3r is coeval with the alternative, more complex version of UT26 (shown next to GPTS-B in Fig. 17). In either case the 'upper part' of the WFm is absent at the hiatus at the base of the CMbr in S-20, with rather less missing for the alternative correlation to UT26. Conversely, a 'lower part' of the WFm must be missing at StAB, with a more limited part missing at its junction with the CMbr (Gallois, 2009), as is implied by the correlated chronometric dates (Fig. 15). In this scenario the Marshi CIE at StAB (Lindström *et al.*, 2017) may be equivalent to the E4 CIE in the Italcementi section (Lombardy) since this is slightly above the equivalent of UT26r in both sections (Fig. 17). The projected age mismatch between the reverse magnetozones SA5n.1r≡E22r in the Newark Supergroup (Fig. 15) is probably due to the imprecise correlation of $\delta^{13}C_{org}$ records between the Peruvian sections and StAB (as in Ruhl *et al.*, 2020, Fig. 3), which locates date LM4 58/59 too low in the correlation to the StAB section (Fig. 15). Rather more is missing from the basal WFm below LP3r.6r≡UT26r at Lavernock (Fig. 16).

The reverse submagnetozone in the base of the CMbr (BM3r.4r ≡SA5n.3r; Fig. 17) is some 7 to 44 cm thick in S-20 and ~5 to 20 cm thick at StAB (ranges from sample spacing). Projecting down the SAR in these sections suggests durations for those

https://doi.org/10.1017/S0016756825100162 Published online by Cambridge University Press

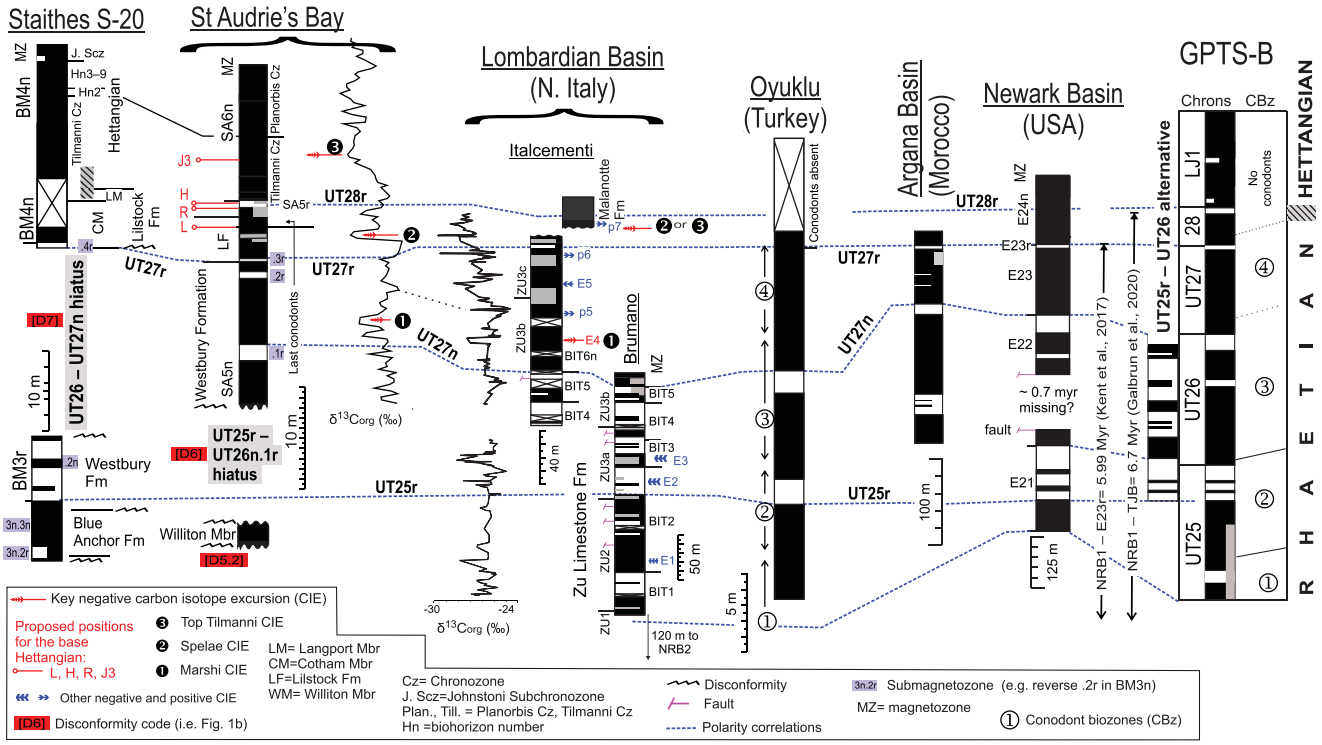

Figure 17. Comparison of the Staithes S-20 core magnetostratigraphy from the Penarth and Lias Groups with other key sections of Rhaetian-2 to early Hettangian age. Other section data: St Audrie's Bay (StAB) (Hounslow *et al.*, 2004, Hesselbo *et al.*, 2002; Hüsing *et al.*, 2014), Lombardian Basin (Muttoni *et al.*, 2010; Zaffani *et al.*, 2018), Oyuklu (Gallet *et al.*, 2007), Argana Basin (Deenan *et al.*, 2011) Newark Basin (Kent *et al.*, 1995, 2017). GPTS-B (Hounslow & Gallois, 2023). Hatching in the S-20 and GPTS-B columns represents uncertainty regarding the position of the Triassic–Jurassic boundary, uncertainty in the StAB column that is shown by the various proposed positions for the boundary, which are labelled: L, R, H and J3, from Lindström *et al.* (2017), Ruhl *et al* (2020), Hillebrandt *et al.* (2013) and Jeram *et al.* (2021), respectively (also in Fig. 3b).

submagnetozones of 2–7 kyr and 2–8 kyr, respectively; these are shorter, but otherwise like the c. 11 kyr is suggested for the coeval E23r in the Newark Supergroup and elsewhere in eastern North America (Blackburn *et al.*, 2013). At StAB the overlying SA5r submagnetozone is some 28–59 cm thick, corresponding to a duration of 12–25 kyr. SA5r is some 28 kyr younger than the base of the Lias Gp and is at a level that was inferred to be near the base Hettangian by Hillebrandt *et al.* (2013), Lindström *et al.* (2017), and Ruhl *et al.* (2020). Using the age anchor for the astrochronology indicates that the base and top of SA5r are 201.32 and 201.28 Ma in age, respectively. Currently, an equivalent of SA5r≡ LP4n.1r (Fig. 16) has not been detected in North America, where it should lie in the middle of the CAMP successions (Fig. 15). Reversed polarity units were reported by Knight *et al.* (2004) in the middle of the CAMP succession in Morocco, but these were refuted by Font *et al.* (2011). Reverse polarity units occur at around 201.5 to 201.3 Ma in the CAMP in Brazil (Moreira *et al.*, 2023), and brief reversals occur in possibly coeval parts of the Montcornet core in the Paris Basin (Yang *et al.*, 1996). Rather rare CAMP dykes with reverse polarity are also known (Smith, 1987; Palencia Ortas *et al.*, 2006). It therefore appears that the equivalent of SA5r≡ LP4n.1r≡ UT28r is still to be clearly recognized in other basins following the initial CAMP eruptions.

5.c. End-Triassic extinction scenarios and synchronicity of CAMP

With the improved chronological and magnetostratigraphic correlation to the initial CAMP basalts provided by this work, the lower part of the Cotham Mbr is clearly coeval with the start of CAMP, some 10 to 20 kyr after the top of E23r≡ SA5n.3r≡ BM3r.4r≡ UT27r (Blackburn *et al.*, 2013). This associates the floral changes in the SAB2 Az in the UK (Fig. 5a) with the start of the crisis interval (Lindström, 2021). Since there is a substantial hiatus between the WFm and the CMbr in S-20 (Fig. 17), the abrupt changes in eco-plant proxies EGT and EPH across this boundary also reflect the time missing at this hiatus.

Scenarios for flood basalt-promoted extinctions are broadly twofold. Firstly, extreme greenhouse conditions caused by large volumes of volcanic CO_2 and associated intrusion-heating of carbon-rich sediments, and secondly, temporary icehouse conditions prompted by large volumes of volcanic-associated SO_2, atmospheric poisoning, associated cooling, and glacioeustatic-forced regression (Self *et al.*, 2006; Schaller *et al.*, 2011; Guex *et al.*, 2016; Algeo & Shen, 2024). Relative temperature estimates from the EGT proxy in S-20 suggest a decline from an interval around or just below the probable Spelae CIE, a rise again near the base of the Lilstock Fm and a further decline into the Redcar Mudstone Fm (Fig. 5c). This broadly corresponds with temperature changes at a similar time inferred at Hochalplgraben (Austria) by Bonis & Kürschner (2012) using spore and pollen data. If this cooling was accompanied by ~16ºC temperature seasonality, as inferred by Petryshyn *et al.* (2020), coincident with the Spelae CIE, this could explain the large increase in eurythermic taxa over the SAB2/SAB3 zonal interval (Fig. 5c). Alternative plausible enhancement mechanisms leading to cooling are SO_2 generation by heating sediments to 300–500ºC caused by CAMP sill and dyke injections (Kaiho *et al.*, 2022) or via sulphur liberated from initial lithospheric melting (Guex *et al.*, 2016). The SO_2 forced cooling scenario seems

https://doi.org/10.1017/S0016756825100162 Published online by Cambridge University Press

to offer a better explanation of our dataset, although the changes observed could reflect regional palaeoclimate, rather than the expected global and/or seawater temperatures, which largely implicate a temperature increase due to CAMP CO_2 inputs (Korte *et al.,* 2009; Algeo & Shen, 2024).

In contrast, the analysis of the StAB section by Bonis & Kürschner (2012) suggests an overall increased temperature from the Spelae CIE, but with a temporary temperature decline in the upper Langport Mbr. This is consistent with a possible ~8ºC temperature increase into the Lias Gp based on $\delta^{18}O$ data from Lavernock (Korte *et al*., 2009) and clumped isotope data from the Cotham Marble (at the Spelae CIE level), which implies no cooling but ~16ºC temperature seasonality (Petryshyn et al., 2020). However, it is not clear that the ordination coordinates derived from the miospore species composition by Bonis & Kürschner (2012) reflect similar environmental responses at both StAB and Hochalplgraben, since the major variance is inferred to have been in temperature at the former and in humidity at the latter. This suggests that the ordination scores may be dominated by local effects at both locations. Probably a more consistent inter-section approach should be applied to miospore data to extract regional responses and reduce local controls (Bhatta *et al*., 2023).

6. Conclusions

The Staithes S-20 magnetostratigraphy indicates that a substantial hiatus exists between the Branscombe Mudstone Fm and the base of the Blue Anchor Fm and that this includes the Norian–Rhaetian boundary interval. This hiatus probably corresponds with the combined D5.1 and D5.2 disconformities of the Germanic Keuper. The Blue Anchor Fm and WFm in S-20 are not synchronous with the equivalent formations in SW England. In S-20, the Blue Anchor Fm is probably equivalent to the youngest (Williton) member of the Blue Anchor Fm in SW England. The WFm in S-20 is older (either late Rhaetian-2 or early Rhaetian-3) than that seen in SW England, which is coeval with late Rhaetian-3 and most of Rhaetian-4. A reverse polarity magnetozone in the basal part of the CMbr in S-20 is coeval with reverse magnetozone SA5n.3r detected at the same stratigraphic level at StAB. Changes in miospore taxa in S-20 are like those at StAB and elsewhere in the UK and include the peak in spore abundance that is typical of the Lilstock Fm and its lateral equivalents. Eco-plant model assessment indicates an increase in humidity in the Lilstock Fm, with increases in eurythermic and euryphyte miospore taxa connected with the peak in spore abundance, followed by cooling into the basal Hettangian.

A joint astrochronology for the earliest Hettangian chronozones from S-20 and the StAB, Lavernock and Lyme Regis sections is anchored to Peruvian radioisotope dates correlated into the StAB section using organic carbon isotope datasets. The astrochronology is anchored on the basal Lias Group at 201.394 Ma. The Tilmanni Cz and Planorbis Scz durations are determined as 262±53 kyrs and 238±27 kyr, respectively, values intermediate between previous estimates.

The anchored astrochronology demonstrates that the reverse magnetozone SA5n.3r (and LBM3r.4r at S-20), in the base of the CMbr, is coeval with magnetozone E23r in the Newark Supergroup, and that the Spelae CIE at StAB and the palynological turnovers are therefore associated with the initial phases of the CAMP. The miospore compositional changes and inferences from the eco-plant model evaluation are consistent with a cooling and enhanced seasonality, conditions prompted by large volumes of CAMP-associated SO_2 and atmospheric poisoning. Alternatively, the miospore changes may reflect a regional response superimposed on a more global warming trend.

Supplementary material. The supplementary material for this article can be found at https://doi.org/10.1017/S0016756825100162

Acknowledgements. Authors MWH and GW were in part supported by Norsk Hydro, Saga Petroleum and Deminex. Dennis Kent is thanked for the use of the palaeomagnetic facilities at Lamont-Doherty Observatory. Staff in the core store at BGS are thanked for facilitating access to the core. Simon Harris (BGS) provided imaging of the core and ammonite specimens. Boulby mine Chief Geologist provided permission for sampling. The reviewers, Sophie Lindström and an anonymous one provided constructive comments.

Data availability. All the data and R scripts used here are either hosted on figshare (Hounslow, 2025) or contained in the Supplementary Material.

Competing interests. The authors declare none.

References

Algeo TJ and Shen J (2024) Theory and classification of mass extinction causation. *National Science Review* 11, https://doi.org/10.1093/nsr/nwad237

Arzani N (2006) Primary versus diagenetic bedding in the limestone-marl/shale alternations of the epeiric seas, an example from the Lower Lias (early Jurassic) of SW Britain. *Carbonates and Evaporites* **21**, 94–109.

Atkinson JW, Wignall PB and Page KN (2020) The Hettangian–Sinemurian (Lower Jurassic) strata of Redcar, Cleveland Basin, NE England: facies and palaeoecology. *Proceedings of the Yorkshire Geological Society* **63**, 77–87.

Bachmann GH, Geluk MC, Warrington G, Becker-Roman A, Beutler G, Hagdorn H, Hounslow MW, Nitsch E, Röhling H-G, Simon T and Szulc A (2010) Triassic. In *Petroleum Geological Atlas of the Southern Permian Basin Area* (eds JC Doornenbal & AG Stevenson), pp. 149–73, Houten (EAGE Publications),

Barnasch J (2010) *Der Keuper im Westteil des Zentraleuropäischen Beckens (Deutschland, Niederlande, England, Dänemark): diskontinuierliche Sedimentation, Litho-, Zyklo-und Sequenzstratigraphie*. Schriftenreihe der Deutschen Gesellschaft für Geowissenschaften, 7–169.

Barnasch J, Geluk MC and Warrington G (2021) A7. Die Trias im westlichen Germanischen Becken: England, Niederlande und Nordsee. In *Trias – Aufbruch in das Erdmittelalter* (eds N Hauschke, M Franz & GH Bachmann), pp. 109–20, Bd. 1, München: Verlag

Barth G, Franz M, Heunisch C, Ernst W, Zimmermann J and Wolfgramm M (2018) Marine and terrestrial sedimentation across the T–J transition in the North German Basin. *Palaeogeography, Palaeoclimatology, Palaeoecology* **489**, 74–94.

Beith SJ, Fox CP, Marshall JE and Whiteside JH (2023) Compound-specific carbon isotope evidence that the initial carbon isotope excursion in the end-Triassic strata in northwest Tethys is not the product of CAMP magmatism. *Global and Planetary Change* **222**, 104044. https://doi.org/10.1016/j.gloplacha.2023.104044

Benton MJ, Cook E and Turner P (2002) Permian and Triassic Red Beds and the Penarth Group of Great Britain. Geological Conservation Review Series, 24, Joint Nature Conservation Committee, Peterborough.

Berger A, Loutre MF and Laskar J (1992) Stability of the astronomical frequencies over the Earth's history for paleoclimate studies, *Science* **255**, 560–66.

Bhatta KP, Mottl O, Felde VA, Flantua SG, Birks HH, Cao X, Chen F, Grytnes JA, Seddon AW and Birks HJB (2023) Exploring spatio-temporal patterns of palynological changes in Asia during the Holocene. *Frontiers in Ecology and Evolution* **11**, 1115784. https://doi.org/10.3389/fevo.2023.1115784

Blackburn TJ, Olsen PE, Bowring SA, McLean NM, Kent DV, Puffer J, McHone G, Rasbury ET and Et-Touhami M (2013) Zircon U-Pb geochronology links the end-Triassic extinction with the Central Atlantic Magmatic Province. *Science* **340**, 941–45.

Bloos G and Page KN (2000) The basal Jurassic ammonite succession in the North-West European Province - Review and new results. In *Advances in*

Jurassic Research 2000 (eds R.L. Hall & P.L. Smith), pp. 27–40, Proceedings of the Fifth International Symposium on the Jurassic System. *GeoResearch Forum*, 6.

Boomer I, Copestake P, Raine R, Azmi A, Fenton JP, Page KN and O'Callaghan M (2021) Stratigraphy palaeoenvironments and geochemistry across the Triassic–Jurassic boundary transition at Carnduff, County Antrim, Northern Ireland. *Proceedings of the Geologists' Association* **132**, 667–87.

Bonis NR (2010) *Palaeoenvironmental changes and vegetation history during the Triassic–Jurassic transition*. PhD thesis, Utrecht University

Bonis NR, Ruhl M and Kürschner WM (2010) Milankovitch-scale palynological turnover across the Triassic–Jurassic transition at St. Audrie's Bay, SW UK. *Journal of the Geological Society* **167**, 877–88.

Bonis NR and Kürschner WM (2012) Vegetation history, diversity patterns, and climate change across the Triassic/Jurassic boundary. *Paleobiology* **38**, 240–64.

Bosmans JHC, Drijfhout SS, Tuenter E, Hilgen FJ, Lourens LJ and Rohling EJ (2015) Precession and obliquity forcing of the freshwater budget over the Mediterranean. *Quaternary Science Reviews* **123**, 16–30.

Bos R, Lindström S, van Konijnenburg-van Cittert H, Hilgen F, Hollaar TP, Aalpoel H, van der Weijst C, Sanei H, Rudra A, Sluijs A and Van de Schootbrugge B (2023) Triassic–Jurassic vegetation response to carbon cycle perturbations and climate change. *Global and Planetary Change* **228**, 104211. https://doi.org/10.1016/j.gloplacha.2023.104211

Bottrell S and Raiswell R (1989) Primary versus diagenetic origin of Blue Lias rhythms (Dorset, UK): evidence from sulphur geochemistry. *Terra Nova* **1**, 451–56.

Brett CE, Allison PA and Hendy AJ (2011) Comparative taphonomy and sedimentology of small-scale mixed carbonate/siliciclastic cycles: Synopsis of Phanerozoic examples. In *Taphonomy* (eds PA Allison & DJ Bottjer), pp.107–98, Geobiology Book Series, no. 32. Springer, Dordrecht.,

Briden JC and Daniels BA (1999) Palaeomagnetic correlation of the Upper Triassic of Somerset, England, with continental Europe and eastern North America. *Journal of the Geological Society* **156**, 317–26.

Cameron TDJ, Crosby A, Balson PS, Jeffrey DH, Lott GK, Bulat J and Harrison DJ (1992) *The geology on the southern North Sea*, United Kingdom offshore regional report. London HMSO for the BGS.

Clémence ME, Bartolini A, Gardin S, Paris G, Beaumont V and Page KN (2010) Early Hettangian benthic–planktonic coupling at Doniford (SW England): Palaeoenvironmental implications for the aftermath of the end-Triassic crisis. *Palaeogeography, Palaeoclimatology, Palaeoecology* **295**, 102–15.

Clemens SC and Prell WL (1991) One million year record of summer monsoon winds and continental aridity from the Owen Ridge (Site 722), Northwest Arabian Sea. In: *Proceedings of the ocean drilling program, Scientific results*,117, 365–388, Ocean Drilling Program College Station.

Courtinat B and Piriou S (2002) Palaeoenvironmental distribution of the Rhaetian dinoflagellate cysts Dapcodinium priscum Evitt, 1961, emend. Below, 1987 and Rhaetogonyaulax rhaetica (Sarjeant) Loeblich and Loeblich, 1976, emend. Harland et al., 1975, emend. Below, 1987. *Geobios* **35**, 429–39.

Deconinck JF, Hesselbo SP, Debuisser N, Averbuch O, Baudin F and Bessa J (2003) Environmental controls on clay mineralogy of an Early Jurassic mudrock (Blue Lias Formation, southern England). *International Journal of Earth Sciences* **92**, 255–66.

Deenen M, Langereis C, Krijgsman W, Hachimi HE and Chellai EH (2011) Palaeomagnetic results from Upper Triassic red-beds and CAMP lavas of the Argana Basin, Morocco. In *The Formation and Evolution of Africa: A Synopsis of 3.8 Ga of Earth History* (eds DJJ van Hinsbergen, SJH Buiter, TH Torsvik, C Gaina, & SJ Webb), pp. 195–209, Geological Society, London, Special Publications no 357.

Elliott RE (1961) The stratigraphy of the Keuper Series in southern Nottinghamshire. *Proceedings of the Yorkshire Geological Society* **33**, 197–234.

Enkin RJ and Watson GS (1996) Statistical analysis of palaeomagnetic inclination data. *Geophysical Journal International* **126**, 495–504.

Font E, Youbi N, Fernandes S, El Hachimi H, Kratinova Z and Hamim Y (2011) Revisiting the magnetostratigraphy of the Central Atlantic Magmatic Province (CAMP) in Morocco. *Earth and Planetary Science Letters* **309**, 302–17.

Fox CP, Cui X, Whiteside JH, Olsen PE, Summons RE and Grice K (2020) Molecular and isotopic evidence reveals the end-Triassic carbon isotope excursion is not from massive exogenous light carbon. *Proceedings of the National Academy of Sciences* **117**, 30171–78, https://doi.org/10.1073/pnas.1917661117

Galbrun B, Boulila S, Krystyn L, Richoz S, Gardin S, Bartolini A and Maslo M (2020) " Short" or" long" Rhaetian? Astronomical calibration of Austrian key sections. *Global and Planetary Change* **192**, 103253. https://doi.org/10.1016/j.gloplacha.2020.103253

Gallet Y, Krystyn L, Marcoux J and Besse J (2007) New constraints on the end-Triassic (Upper Norian–Rhaetian) magnetostratigraphy. *Earth and Planetary Science Letters* **255**, 458–70.

Gallois RW (2001) The lithostratigraphy of the Mercia mudstone group (mid–late Triassic) of the south Devon coast. *Geoscience in south-west England-Proceedings of the Ussher Society* **10**, 195–204.

Gallois RW (2007) The stratigraphy of the Penarth Group (late Triassic) of the east Devon coast. Geoscience in South-West England. *Geoscience in south-west England-Proceedings of the Ussher Society* **11**, 287–97.

Gallois RW (2009) The lithostratigraphy of the Penarth Group (late Triassic) of the Severn Estuary area. Geoscience in South-West England. *Geoscience in south-west England-Proceedings of the Ussher Society* **12**, 71–84.

Geluk M.C (2005) *Stratigraphy and tectonics of Permo–Triassic basins in the Netherlands and surrounding areas*. PhD thesis, Utrecht University.

Guex J, Schoene B, Bartolini A, Spangenberg J, Schaltegger U, O'Dogherty L, Taylor D, Bucher H and Atudorei V (2012) Geochronological constraints on post-extinction recovery of the ammonoids and carbon cycle pertur bations during the Early Jurassic. *Palaeogeography, Palaeoclimatology, Pala eoecology* **346**, 1–11.

Guex J., Pilet S., Müntener O., Bartolini A., Spangenberg J., Schoene B., Sell B. and Schaltegger U (2016) Thermal erosion of cratonic lithosphere as a potential trigger for mass-extinction. *Scientific Reports* **6**, 23168. https://doi.org/10.1038/srep23168

Gravendyk J (2021) *Shedding new light on the Triassic–Jurassic, transition in the Germanic Basin*. PhD thesis, Freie Universität Berlin.

Gravendyck J, Schobben M, Bachelier JB and Kürschner WM (2020) Macroecological patterns of the terrestrial vegetation history during the end-Triassic biotic crisis in the central European basin: a palynological study of the Bonenburg section (NW-Germany) and its supra-regional implications. *Global and Planetary Change* **194**, 103286. https://doi.org/10.1016/j.gloplacha.2020.103286

Hailwood EA and Ding F (1995) Palaeomagnetic reorientation of cores and the magnetic fabric of hydrocarbon reservoir sands. In *Palaeomagnetic Applications in Hydrocarbon Exploration and Production* (eds P Turner & A Turner), pp.245–58, Geological Society, London, Special Publications no. 98.

Hesselbo SP, Robinson SA, Surlyk F and Piasecki S (2002) Terrestrial and marine extinction at the Triassic–Jurassic boundary synchronized with major carbon-cycle perturbation: a link to initiation of massive volcanism? *Geology* **30**, 251–54.

Hesselbo SP, Al-Suwaidi A Baker SJ, *et al.* (2023) Initial results of coring at Prees, Cheshire Basin, UK (ICDP JET project): towards an integrated stratigraphy, timescale, and Earth system understanding for the Early Jurassic. *Scientific Drilling* **32**, 1–25, https://doi.org/10.5194/sd-32-1-2023

Hilgen FJ, Hinnov LA, Abdul Aziz H, Abels H.A., Batenburg S, Bosmans JH, de Boer B, Hüsing SK, Kuiper KF, Lourens LJ and Rivera T (2015) Stratigraphic continuity and fragmentary sedimentation: the success of cyclostratigraphy as part of integrated stratigraphy. In *Strata and Time: Probing the Gaps in Our Understanding* (eds DG Smith, RJ Bailey, PM Burgess & AJ Fraser), pp. 57–197, The Geological Society of London, special publicayion no. 404.

Hillebrandt AV and Krystyn L (2009) On the oldest Jurassic ammonites of Europe (Northern Calcareous Alps, Austria) and their global significance. *Neues Jahrbuch für Geologie und Paläontologie* **253**, 163–95.

Hillebrandt AV, Krystyn L, Kürschner WM, Bonis NR, Ruhl M, Richoz S, Schobben MAN, Urlichs M, Bown PR, Kment K and McRoberts CA

https://doi.org/10.1017/S0016756825100162 Published online by Cambridge University Press

(2013) The global stratotype sections and point (GSSP) for the base of the Jurassic System at Kuhjoch (Karwendel Mountains, Northern Calcareous Alps, Tyrol, Austria). *Episodes* **36**, 162–98. https://doi.org/10.18814/epiiugs/2013/v36i3/001

Hodges P (2021) A new ammonite from the Penarth Group, South Wales and the base of the Jurassic System in SW Britain. *Geological Magazine* **158**, 1109–14.

Hounslow MW (1985) Magnetic fabric arising from paramagnetic phyllosilicate minerals in mudrocks. *Journal of the Geological Society* **142**, 995–1006.

Hounslow MW, (2023) *Palaeomag-Tools, Version 5.1a*. figshare. Software. https://doi.org/10.6084/m9.figshare.24167190.v1

Hounslow MW (2025) Palaeomagnetic and astrochronologic dataset for the Staithes S-20 core, and the joint Tillmanni plus Planorbis chronozone astrochronology. figshare. Dataset. https://doi.org/10.6084/m9.figshare.26046514.

Hounslow MW and Muttoni G (2010) The geomagnetic polarity timescale for the Triassic: linkage to stage boundary definitions. In *The Triassic Timescale* (ed SG Lucas), pp. 61–102, Geological Society, London, Special Publications no. 334.

Hounslow MW and Gallois R (2023) Magnetostratigraphy of the Mercia Mudstone Group (Devon, UK): implications for regional relationships and chronostratigraphy in the Middle to Late Triassic of western Europe. *Journal of the Geological Society* **180**, jgs2022–173. –https://doi.org/10.1144/jgs2022–173.

Hounslow MW and Andrews JE (2024) Coupled magneto- and carbon isotope- stratigraphy of SW British Rhaetian improves regional chronostratigraphy and fine tunes timing of Late Triassic global environmental changes. *Palaeogeography, Palaeoclimatology, Palaeoecology* **656**, 112579. https://doi.org/10.1016/j.palaeo.2024.112579.

Hounslow MW, Posen PE and Warrington G (2004) Magnetostratigraphy and biostratigraphy of the Upper Triassic and lowermost Jurassic succession, St. Audrie's Bay, UK. *Palaeogeography, Palaeoclimatology, Palaeoecology* **213**, 331–58.

Howard A, Warrington G, Ambrose K and Rees J (2008) A formational framework for the Mercia Mudstone Group (Triassic) of England and Wales. British Geological Survey Research Report, RR/08/04.

Howarth MK (1962) The Yorkshire type ammonites and nautiloids of Young and Bird, Phillips, and Martin Simpson. *Palaeontology* **5**, 93–136.

Howarth MK (2002) The lower Lias of Robin Hood's Bay, Yorkshire, and the work of Leslie Bairstow. *Bulletin of the Natural History Museum London (Geology)* **58**, 81–152. https://doi.org/10.1017/S0968046202000037

Hüsing SK, Hilgen FJ, Abdul Aziz H and Krijgsman W (2007) Completing the Neogene geological time scale between 8.5 and 12.5 Ma. *Earth and Planetary Science Letters* **253** 340–58. https://doi.org/10.1016/j.epsl.2006.10.036.

Hüsing SK, Beniest A, van der Boon A, Abels HA, Deenen MHL, Ruhl M and Krijgsman W (2014) Astronomically-calibrated magnetostratigraphy of the Lower Jurassic marine successions at St. Audrie's Bay and East Quantoxhead (Hettangian–Sinemurian; Somerset, UK). *Palaeogeography, Palaeoclimatology, Palaeoecology* **403**, 43–56.

Ivimey-Cook HC and Powell JH (1991) Late Triassic and Early Jurassic biostratigraphy of the Felixkirk borehole, North Yorkshire. *Proceedings of the Yorkshire Geological Society* **48**, 367–74.

Jeans CV (1995) Clay mineral stratigraphy in Palaeozoic and Mesozoic red bed facies onshore and offshore UK. In *Non-biostratigraphical Methods of Dating and Correlation* (eds RE Dunay & EA Hailwood), pp. 31–55, Geological Society, London, Special Publications no. 89.

Jeans CV, Mitchell JG, Scherer M and Fisher MJ (1994) Origin of the Permo–Triassic clay mica assemblage. *Clay Minerals* **29**, 575–89.

Jeram AJ, Simms MJ, Hesselbo SP and Raine R (2021) Carbon isotopes, ammonites and earthquakes: key Triassic–Jurassic boundary events in the coastal sections of south-east County Antrim, Northern Ireland, UK. *Proceedings of the Geologists' Association* **132**, 702–25.

Johnson H, Warrington G and Stoker SJ (1994) Permian and Triassic of the Southern North Sea. In: *Lithostratigraphic Nomenclature of the UK Southern North Sea* (eds RWO'B Knox, & WG Cordey,), Nottingham: British Geological Survey.

Kaiho K, Tanaka D, Richoz S, Jones DS, Saito R, Kameyama D, Ikeda M, Takahashi S, Aftabuzzaman M and Fujibayashi M (2022) Volcanic temperature changes modulated volatile release and climate fluctuations at the end-Triassic mass extinction. *Earth and Planetary Science Letters* **579**, 117364. https://doi.org/10.1016/j.epsl.2021.117364

Kent DV, Olsen PE and Witte WK (1995) Late Triassic-earliest Jurassic geomagnetic polarity sequence and paleolatitudes from drill cores in the Newark rift basin, eastern North America. *Journal of Geophysical Research: Solid Earth* **100**, 14965–98.

Kent DV, Olsen PE and Muttoni G (2017) Astrochronostratigraphic polarity time scale (APTS) for the Late Triassic and Early Jurassic from continental sediments and correlation with standard marine stages. *Earth-Science Reviews* **166**, 153–80.

Kent JT, Briden JC and Mardia KV (1983) Linear and planar structure in ordered mulivariate data as applied to progressive demagnetisation of palaeomagnetic remanance. *Geophysical Journal of the Royal Astronomical Society* **81**, 75–87.

Kent PE (1953) The Rhaetic beds of the north-east midlands. *Proceedings of the Yorkshire Geological Society* **29**, 117–39.

Kent PE (1968) The Rhaetic beds. In: *The geology of the East Midlands* (eds PC Sylvester-Bradley, TD Ford (eds). pp. 174–187. Leicester Univ. Press.

Kment K (2021) Biostratigraphy of the Hettangian Stage in the Northern Calcareous Alps (Austria, Bavaria) with ammonoids and their classification into biohorizons. *Neues Jahrbuch fur Geolologie Palaontologie Abhandlungen* **301**, 233–82, https://doi.org/10.1127/njgpa/2021/1007

Knight KB, Nomade S, Renne PR, Marzoli A, Bertrand H and Youbi N (2004) The Central Atlantic Magmatic Province at the Triassic–Jurassic boundary: paleomagnetic and 40Ar/39Ar evidence from Morocco for brief, episodic volcanism. *Earth and Planetary Science Letters* **228**, 143–60.

Korte C, Hesselbo SP, Jenkyns HC, Rickaby RE and Spötl C (2009) Palaeoenvironmental significance of carbon-and oxygen-isotope stratigraphy of marine Triassic–Jurassic boundary sections in SW Britain. *Journal of the Geological Society* **166**, 431–45.

Korte C, Ruhl M, Palfy J, Ullmann CV and Hesselbo SP (2019) Chemostratigraphy across the Triassic–Jurassic boundary. In *Chemostratigraphy Across Major Chronological Boundaries* (eds AN Sial, C Gaucher, M Ramkumar, VP Ferreira), pp. 185–210,. Geophysical Monograph no. 240. American Geophysical Union, John Wiley.

Krystyn L (2008) An ammonoid-calibrated Tethyan conodont time scale of the late Upper Triassic. *Berichte der Geologischen Bundesanstalt* **76**, 9–11.

Krystyn L, Richoz S, Gallet Y, Bouquerel H, Kürschner WM and Spötl C (2007) Updated bio-and magnetostratigraphy from Steinbergkogel (Austria), candidate GSSP for the base of the Rhaetian stage. *Albertiana* **36**, 164–73.

Kürschner WM and Herngreen GW (2010) Triassic palynology of central and northwestern Europe: a review of palynofloral diversity patterns and biostratigraphic subdivisions. In *The Triassic Timescale* (ed SG Lucas), pp. 263–83, Geological Society, London, Special Publications no. 334.

Lindström S (2016) Palynofloral patterns of terrestrial ecosystem change during the end-Triassic event – a review. *Geological Magazine* **153**, 223–51

Lindström S (2021) Two-phased mass rarity and extinction in land plants during the end-Triassic climate crisis. *Frontiers in Earth Science* **9**, 780343. https://doi.org/10.3389/feart.2021.780343

Lindström S and Erlström M (2006) The late Rhaetian transgression in southern Sweden: Regional (and global) recognition and relation to the Triassic–Jurassic boundary. *Palaeogeography, Palaeoclimatology, Palaeoecology* **241**, 339–72.

Lindström S, Van de Schootbrugge B, Hansen KH, Pedersen GK, Alsen P, Thibault N, Dybkjær K, Bjerrum CJ and Nielsen LH (2017) A new correlation of Triassic–Jurassic boundary successions in NW Europe, Nevada and Peru, and the Central Atlantic Magmatic Province: a time-line for the end-Triassic mass extinction. *Palaeogeography, Palaeoclimatology, Palaeoecology* **478**, 80–102.

Lindström S, Pedersen GK, Vosgerau H, Hovikoski J, Dybkjær K and Nielsen LH (2023) Palynology of the Triassic–Jurassic transition of the Danish Basin (Denmark): a palynostratigraphic zonation of the Gassum–lower Fjerritslev formations. *Palynology* **47**, 2241068. https://doi.org/10.1080/01916122.2023.2241068.

Lott GK and Warrington G (1988) A review of the latest Triassic succession in the U.K. sector of the southern North Sea Basin. *Proceedings of the Yorkshire Geological Society* **42**, 139–47.

Mayall MJ (1981) The Late Triassic Blue Anchor formation and the initial Rhaetian marine transgression in south-west Britain. *Geological Magazine* **118**, 377–84.

McKie T (2014) Climatic and tectonic controls on Triassic dryland terminal fluvial system architecture, central North Sea. In *Depositional Systems to Sedimentary Successions on the Norwegian Continental Margin* (eds AW Martinius, R Ravnås, J.A Howell, RJ Steel, & JP Wonham), pp.19–57, International Association of Sedimentologists, Wiley and Sons,

Meyers SR (2014) *Astrochron: An R Package for Astrochronology*. https://cran.r-project.org/package=astrochron

Meyers SR (2015) The evaluation of eccentricity-related amplitude modulation and bundling in paleoclimate data: An inverse approach for astrochronologic testing and time scale optimization. *Paleoceanography, Palaeoclimatology* **30**, 1625–40.

Meyers SR (2019) Cyclostratigraphy and the problem of astrochronologic testing. *Earth-Science Reviews* **190**, 190–223.

Meyers SR and Sageman BB (2004) Detection, quantification, and significance of hiatuses in pelagic and hemipelagic strata. *Earth and Planetary Science Letters* **224**, 55–72.

Meyers SR and Malinverno A (2018) Proterozoic Milankovitch cycles and the history of the solar system. *Proceedings of the National Academy of Sciences* **115**, 6363–68.

Meyers SR, Sageman BB and Hinnov LA (2001) Integrated quantitative stratigraphy of the Cenomanian–Turonian Bridge Creek Limestone Member using evolutive harmonic analysis and stratigraphic modelling. *Journal of Sedimentary Research* **71**, 628–44.

Moghadam HV and Paul CRC (2000) Trace fossils of the Jurassic, Blue Lias, Lyme Regis, southern England. *Ichnos: An International Journal of Plant & Animal* **7**, 283–306.

Montgomery P, Hailwood EA, Gale AS and Burnett JA (1998) The magnetostratigraphy of Coniacian–Late Campanian chalk sequences in southern England. *Earth and Planetary Science Letters* **156**, 209–24.

Moreira G, Ernesto M, De Min A, Marzoli A, Machado FB, Vasconcellos EMG and Bellieni G (2023) Paleomagnetism of the Penatecaua magmatism: The CAMP intrusive rocks in the Amazonas Basin, northern Brazil. *Physics of the Earth and Planetary Interiors* **342**, 107075. https://doi.org/10.1016/j.pepi.2023.107075

Muttoni G, Kent DV, Jadoul F, Olsen PE, Rigo M, Galli MT and Nicora A (2010) Rhaetian magneto-biostratigraphy from the Southern Alps (Italy): constraints on Triassic chronology. *Palaeogeography, Palaeoclimatology, Palaeoecology* **285**, 1–16.

Olsen PE, Kent DV, Cornet B, Witte WK and Schlische RW (1996) High-resolution stratigraphy of the Newark rift basin (early Mesozoic, eastern North America). *Geological Society of America Bulletin* **108**, 40–77.

Omar H, Da Silva AC and Yaich C (2021) Linking the variation of sediment accumulation rate to short term sea-level change using cyclostratigraphy: case study of the Lower Berriasian Hemipelagic Sediments in Central Tunisia (Southern Tethys). *Frontiers in Earth Science* **9**, 638441. https://doi.org/10.3389/feart.2021.638441

Orbell G (1973) Palynology of the British Rhaeto-Liassic. *Bulletin Geological Survey of Great Britain* **44** 1–39.

Page KN (2003) The Lower Jurassic of Europe: its subdivision and correlation. *GEUS Bulletin* **1**, 21–59.

Page KN (2010) Stratigraphical framework. In *Fossils from the Lower Lias of the Dorset coast*, (eds AR Lord, & PG Davis,), Palaeontological association field guide to fossils, **13**, pp.33–53.

Page KN (2017) From Oppel to Callomon (and beyond): building a high-resolution ammonite-based biochronology for the Jurassic System. *Lethaia* **50**, 336–55, https://doi.org/10.1111/let.12209

Palencia Ortas A, Osete ML, Vegas R and Silva P (2006) Paleomagnetic study of the Messejana Plasencia dyke (Portugal and Spain): a lower Jurassic paleopole for the Iberian plate. *Tectonophysics* **420**, 455–72.

Paul CRC, Allison PA and Brett CE (2008) The occurrence and preservation of ammonites in the Blue Lias FormationPaukl (lower Jurassic) of Devon and Dorset, England and their palaeoecological, sedimentological and diagenetic significance. *Palaeogeography, Palaeoclimatology, Palaeoecology* **270**, 258–72.

Petryshyn VA, Greene S.E., Farnsworth A., Lunt DJ, Kelley A, Gammariello R, Ibarra Y, Bottjer DJ, Tripati A and Corsetti FA (2020) The role of temperature in the initiation of the end-Triassic mass extinction. *Earth-Science Reviews* **208**, 103266. https://doi.org/10.1016/j.earscirev.2020.103266

Phillips J (1829) *Illustrations of the Geology of Yorkshire: Part 1- The Yorkshire Coast*. John Murray, London.

Poulsen NE (1996) Dinoflagellate cysts from marine Jurassic deposits of Denmark and Poland. *American Association of Stratigraphic Palynologists, contribution Series* **31**, 226.

Powell JH (1986) Lithostratigraphical nomenclature of the Lias Group in the Yorkshire Basin. *Proceedings of the Yorkshire Geological Society* **45**, 51–57, https://doi.org/10.1144/pygs.45.1-2.51

R Core Team, (2013) R: A language and environment for statistical computing. R Foundation for Statistical Computing, Vienna, Austria.

Reed BC (1989) Linear least-squares fits with errors in both coordinates. *American Journal of Physics* **57**, 642–46.

Rigo M, Bertinelli A, Concheri G, Gattolin G., Godfrey L, Katz ME, Maron M, Mietto P, Muttoni G, Sprovieri M and Stellin F (2016) The Pignola-Abriola section (southern Apennines Italy): a new GSSP candidate for the base of the Rhaetian Stage. *Lethaia* **49** 287–306.

Rigo M, Mazza M, Karádi V and Nicora A (2018) New Upper Triassic conodont biozonation of the Tethyan realm. In *The Late Triassic World* (ed. L Tanner) Springer Cham, pp.189–235. https://doi.org/10.1007/978-3-319-68009-5_6

Ruhl M, Deenen MHL, Abels HA, Bonis NR, Krijgsman W and Kürschner WM (2010) Astronomical constraints on the duration of the early Jurassic Hettangian stage and recovery rates following the end-Triassic mass extinction (St Audrie's Bay/East Quantoxhead, UK). *Earth and Planetary Science Letters* **295**, 262–76.

Ruhl M, Hesselbo SP, Hinnov L, Jenkyns HC, Xu W, Riding JB, Storm M, Minisini D, Ullmann CV and Leng MJ (2016) Astronomical constraints on the duration of the Early Jurassic Pliensbachian Stage and global climatic fluctuations. *Earth and Planetary Science Letters* **455**, 149–65.

Ruhl M, Hesselbo SP, Al-Suwaidi A, Jenkyns HC, Damborenea SE, Manceñido MO, Storm M, Mather TA and Riccardi AC (2020) On the onset of Central Atlantic Magmatic Province (CAMP) volcanism and environmental and carbon-cycle change at the Triassic–Jurassic transition (Neuquén Basin, Argentina). *Earth-Science Reviews* **208**, 103229. https://doi.org/10.1016/j.earscirev.2020.103229

Salisbury J, Gröcke DR, Cheung HA, Kump LR, McKie T and Ruffell A (2022) An 80-million-year sulphur isotope record of pyrite burial over the Permian–Triassic. *Scientific reports* **12**, 17370. https://doi.org/10.1038/s41598-022-21542-4

Salisbury J, Gröcke DR and McKie T (2023) Sulphur isotope stratigraphy of drill cuttings and stratigraphic correlation of Permian-Triassic evaporites. *Frontiers in Earth Science: Sedimentology, Stratigraphy and Diagenesis* **11**, 1216365. https://doi.org/10.3389/feart.2023.1216365

Schaller MF, Wright JD and Kent DV (2011) Atmospheric pCO_2 perturbations associated with the Central Atlantic Magmatic Province. *Science* **331**, 1404–09.

Self S, Widdowson M, Thordarson T and Jay AE (2006) Volatile fluxes during flood basalt eruptions and potential effects on the global environment: a Deccan perspective. *Earth and Planetary Science Letters* **248**, 518–32.

Sheppard TH, Houghton RD and Swan AR (2006) Bedding and pseudo-bedding in the Early Jurassic of Glamorgan: deposition and diagenesis of the Blue Lias in South Wales. *Proceedings of the Geologists' Association* **117**, 249–64.

Smith WA (1987) Paleomagnetic results from a crosscutting system of northwest and north–south trending diabase dikes in the North Carolina Piedmont. *Tectonophysics* **136**, 137–50.

Southworth C (1987) *Lithostratigraphy and depositional history of the Middle Triassic Dowsing Dolomitic Formation of the Southern North Sea and adjoining areas*, PhD dissertation, University of Oxford.

Strasser A (2018) Cyclostratigraphy of shallow-marine carbonates–limitations and opportunities. In *Stratigraphy and Timescales (Vol. 3), Cyclostratigraphy*

and Astrochronology (ed. M. Montenari), pp. 151–87, Academic Press. https://doi.org/10.1016/bs.sats.2018.07.001

Taylor SR (1982) *The Trent, Glen Parva and Blue Anchor formations (upper Triassic) of the east midlands and their sulphate deposits*. PhD thesis, University of Leicester.

Van de Schootbrugge B, Tremolada F, Rosenthal Y, Bailey TR, Feist-Burkhardt S, Brinkhuis H, Pross J, Kent DV and Falkowski PG (2007) End-Triassic calcification crisis and blooms of organic-walled 'disaster species'. *Palaeogeography, Palaeoclimatology, Palaeoecology* **244**, 126–41.

Van de Schootbrugge B, Quan TM, Lindström S, Püttmann W, Heunisch C, Pross J, Fiebig J, Petschick R, Röhling HG, Richoz S and Rosenthal Y (2009) Floral changes across the Triassic/Jurassic boundary linked to flood basalt volcanism. *Nature Geoscience* **2**, 589–94.

Warrington G and Whittaker A (1984) The Blue Anchor Formation (late Triassic) in Somerset. *Proceedings of the Ussher Society* **6**, 100–07.

Warrington G (1997) The Penarth Group–Lias Group succession (Late Triassic–Early Jurassic) in the East Irish Sea Basin and neighbouring areas: a stratigraphical review. In *Petroleum Geology of the Irish Sea and Adjacent Area* (eds NS Meadows, SR Trueblood, M Hardman, G Cowan). pp. 33–46, Geological Society, London, Special Publications no. 124.

Waters RA and Lawrence DJD (1987) Geology of the South Wales Coalfield, Part III, the country around Cardiff. Memoir of the British Geological Survey, England and Wales. London: Her Majesty's Stationery Office.

Weedon GP (1986) Hemipelagic shelf sedimentation and climatic cycles: the basal Jurassic (Blue Lias) of South Britain. *Earth and Planetary Science Letters* **76**, 321–35.

Weedon GP, Jenkyns HC, Coe AL and Hesselbo SP (1999) Astronomical calibration of the Jurassic time-scale from cyclostratigraphy in British mudrock formations. *Philosophical Transactions of the Royal Society of London. Series A: Mathematical, Physical and Engineering Sciences* **357**, 1787–813.

Weedon GP, Jenkyns HC and Page KN (2018) Combined sea-level and climate controls on limestone formation, hiatuses and ammonite preservation in the Blue Lias Formation, South Britain (uppermost Triassic–Lower Jurassic). *Geological Magazine* **155**, 1117–49.

Weedon GP, Page KN and Jenkyns HC (2019) Cyclostratigraphy, stratigraphic gaps and the duration of the Hettangian Stage (Jurassic): insights from the Blue Lias Formation of southern Britain. *Geological Magazine* **156**, 1469–509.

Westphal H, Munnecke A, Böhm F and Bornholdt S (2008) Limestone–marl alternations in epeiric sea settings—witnesses of environmental changes or diagenesis. In *Dynamics of Epeiric Seas: Sedimentological, Paleontological and Geochemical Perspectives* (eds, TJ Algeo, PH Heckel, JB Maynard, R Blakey, H Rowe, BR Pratt, C Holmden), pp. 389–406, Geological Association of Canada Special Publication no. 48.

Whiteside JH, Olsen PE, Eglinton T, Brookfield ME and Sambrotto RN (2010) Compound-specific carbon isotopes from Earth's largest flood basalt eruptions directly linked to the end-Triassic mass extinction. *Proceedings of the National Academy of Sciences* **107**, 6721–25.

Woods PJE (1973) Potash exploration in Yorkshire: Boulby mine pilot borehole. *Transactions (Section B) Institution of Mining and Metallurgy* **82**, 99–106.

Wotzlaw JF, Guex J., Bartolini A, Gallet Y, Krystyn L, McRoberts CA, Taylor D, Schoene B and Schaltegger U (2014) Towards accurate numerical calibration of the Late Triassic: High-precision U-Pb geochronology constraints on the duration of the Rhaetian. *Geology* **42**, 571–74. https://doi.org/10.1130/G35612.1

Xu W, Ruhl M, Hesselbo SP, Riding JB and Jenkyns HC (2017) Orbital pacing of the Early Jurassic carbon cycle, black-shale formation and seabed methane seepage. *Sedimentology* **64**, 127–49.

Yager JA, West AJ, Thibodeau AM, Corsetti FA, Rigo M., Berelson WM, Bottjer DJ, Greene SE, Ibarra Y., Jadoul F and Ritterbush KA (2021) Mercury contents and isotope ratios from diverse depositional environments across the Triassic–Jurassic Boundary: Towards a more robust mercury proxy for large igneous province magmatism. *Earth-Science Reviews* **223**, 103775. https://doi.org/10.1016/j.earscirev.2021.103775

Yang Z, Moreau MG, Bucher H, Dommergues JL and Trouiller A (1996) Hettangian and Sinemurian magnetostratigraphy from the Paris Basin. *Journal Geophysical Research* **101**, 8025–42.

Zaffani M, Jadoul F and Rigo M (2018) A new Rhaetian $\delta^{13}C_{org}$ record: carbon cycle disturbances, volcanism, end-Triassic mass extinction. *Earth-Science Reviews* **178**, 92–104.

Zhang J, Lenz OK, Wang P and Hornung J (2021) The Eco-Plant model and its implication on Mesozoic dispersed sporomorphs for Bryophytes, Pteridophytes, and Gymnosperms. *Review of Palaeobotany and Palynology* **293**, 104503. https://doi.org/10.1016/j.revpalbo.2021.104503

Zhou M, Wu H, Hinnov LA, Fang Q, Zhang S, Yang T and Shi M (2022) Empirical reconstruction of Earth-Moon and solar system dynamical parameters for the past 2.5 billion years from cyclostratigraphy. *Geophysical Research Letters* **49**, e2022GL098304. https://doi.org/10.1029/2022GL098304.